Ph.D. DISSERTATION

Carbon Dioxide Detection Based on FET Platforms at Low Temperature

FET 플랫폼을 기반으로 한 저온에서의 이산화탄소 감지

BY

MEILE WU

February 2019

DEPARTMENT OF ELECTRICAL AND
COMPUTER ENGINEERING
COLLEGE OF ENGINEERING
SEOUL NATIONAL UNIVERSITY

Carbon Dioxide Detection Based on FET Platforms at Low Temperature

FET 플랫폼을 기반으로 한 저온에서의 이산화탄소 감지

지도교수 이 종 호

이 논문을 공학박사 학위논문으로 제출함

2019 년 2 월

서울대학교 대학원

전기정보공학부

우 메 이 레

우메이레의 공학박사 학위논문을 인준함

2019 년 2 월

위 원 장 : 박 병 국 (인)

부위원장 : 이 종 호 (인)

위 원 : 황 철 성 (인)

위 원 : 장 호 원 (인)

위 원 : 권 혁 인 (인)

Carbon Dioxide Detection Based on FET Platforms at Low Temperature

by

Meile Wu

Advisor: Jong-Ho Lee

A dissertation submitted in partial fulfillment of

the requirements for the degree of

Doctor of Philosophy

(Electrical and Computer Engineering)

in Seoul National University

February 2019

Doctoral Committee:

Professor Byung-Gook Park, Chair

Professor Jong-Ho Lee, Vice-Chair

Professor Cheol Seong Hwang

Associate Professor Ho Won Jang

Associate Professor Hyuck-In Kwon

ABSTRACT

In the past few decades, carbon dioxide (CO_2) monitoring and controlling have attracted a lot of attentions. The monitoring of CO_2 outdoor helps researchers to know the change in the quality of the atmospheric air and provides important data for environment research. In the aspect of indoor air quality controlling, it is also important to detect and restrain the CO_2 concentration under a certain level, because high CO_2 concentration indoor can trigger symptoms and affect human health. By now, many efforts have been made to develop reliable CO_2 sensors with long life time, low cost, small size, low power consumption, and low working temperature. Moreover, integratable CO_2 sensor is desired in order to manufacture gas arrays that are compatible with silicon CMOS technology, and extend its application in the field of portable electronic nose system.

In this dissertation, the CO_2 sensors based on FET platforms working at low temperature are investigated. Several kinds of sensing materials are applied to FET platforms, including Polyvinyl alcohol (PVA) polymer, polyethylenimine (PEI)

coated single-walled carbon nanotubes (SWNT) random network, and inorganic Na^+ ionic conducting material. All kinds of the sensing material are deposited on the FET platform by using inkjet printing process. The basic electrical and CO_2 sensing properties of these sensors are measured. The sensing mechanisms are also explained and modeled. PVA and PEI coated SWNT CO_2 sensors are found to be able to detect CO_2 at room temperature (about 25ºC) with the help of water vapor. The sensor with Na^+ ionic conducting material can detect CO_2 at 160ºC. all the sensors proposed in this work have much relative lower working temperature compared to typical CO_2 sensors. The FET platform makes the sensor compatible with Si CMOS technology. A floating gate is adopted in the FET component which makes the calibration of the sensor very convenient. By comparison, the sensor with Na^+ ionic conducting material has the most stable sensing behaviors without the requirement of water vapor during the detection, and can be expected to be a promising candidate for low temperature CO_2 detection.

Keywords: carbon dioxide sensor, FET sensor, low temperature, polymer,

single-walled carbon nanotubes (SWNT), sodium ionic conducting material.

Student number: 2015-30749

CONTENTS

Abstract.....i

Contents.....iv

List of Figures.....vii

List of Tables.....xv

Chapter 1

Introduction.....1

1.1 Study background.....1

1.1.1 Carbon dioxide monitoring and controlling.....1

1.1.2 Gas sensors based on FET platforms.....12

1.2 Purpose of research.....16

1.3 Dissertation outline.....17

Chapter 2

Device structure and fabrication.....18

2.1 FET platform structure and fabrication.....18

2.2 Sensing materials deposition.....23

2.2.1 Organic polymer based sensing material.....23

2.2.2 Carbon based sensing material.....26

2.2.3 Sodium ionic conducting sensing material.....29

2.3 Gas sensing measurement system.....34

Chapter 3

Measurement results.....37

3.1 PVA CO_2 sensor.....37

3.2 PEI-SWNT CO_2 sensor.....43

3.3 Na^+ ionic conducting CO_2 sensor.....53

3.3.1 APTES SAM ion-blocking layer.....54

3.3.2 Gas sensing performance.....63

3.3.3 Programming of the FET sensor platform.....65

Chapter 4

Device sensing mechanism.....69

4.1 Sensing mechanism of PEI-SWNT sensor.....69

4.2 Sensing mechanism of the sensor based on Na^+ conducting material.....76

Chapter 5

Conclusion.....82

Bibliography.....84

Abstract in Korean.....91

List of Publications.....93

List of Figures

Figure 1.1 Change in concentration of CO_2 in air over time [5]. (a) CO_2 concentration record from the year of 1700 to present. (b) CO_2 concentration record from 1958 to present. 7

Figure 1.2 Typical CO_2 levels indoor and their effects on human beings [6]. 8

Figure 1.3 The schematic diagram of optical CO_2 sensor with a straight light path (a) [8], a folded reflection (b) and a multiple reflection (c) [9]. The PD in the figure refers to the photodiode. 9

Figure 1.4 Examples of electrochemical CO_2 sensors. (a) Potentiometric sensor [18]. (b) Amperometric sensor [19]. 11

Figure 1.5. Lundström FET H_2 sensor. (a) Shematic of the sensor [25]. (b) The V_{th} of the FET is changed by H_2 gas. 14

Figure 1.6. Suspended gate (SG) FET sensor with an air gap [25]. 14

Figure 1.7. Capacitively-controlled (CC) FET sensor with a floating gate [27]. 15

Figure 1.8 FET sensor platform having a horizontal floating gate and control gate [28]. (a) The SEM image of the sensor. (b) The cross sectional view cut along line A-A' in (a). 15

Figure 2.1. (a) SEM top view of sensor platform. (b) Schematic cross sectional view cut along A-A'. (c) Schematic cross sectional view cut along B-B'. 21

Figure 2.2. The main fabrication flow of the FET substrate. (a) Silicon wafer with patterned Si_3N_4/SiO_2. (b) The FG is patterned. (c) ONO stack is deposited to cover the whole substrate. (d) Electrodes are patterned. (e) The SU-8 layer is deposited and patterned to expose the interdigitated FG-CG and electrode pads only. (f) The sensor with sensing material. 22

Figure 2.3. PVA ink obtained by dissolving PVA powders in the mixture of DI water and DMOS (4:1 in volume). 25

Figure 2.4. (a) Printed PVA ink on the FET sensor substrate. (b) Capture of the ink

flow printed from the ink cartridge. 25

Figure 2.5. (a) the platform used for the sensors having carbon based sensing materials. (b) and (c) show the images of printed pure SWNT random network and PEI-SWNT. (e) and (f) show the schematic 2D cross sectional view of the sensors with pure SNWT and PEI-SWNT cut alone line A-A' in (a), illustrating the dispersion of the nanotubes by PEI. 28

Figure 2.6. (a) The initial substrate (SiO_2 covered silicon substrate) and its water contact angle. (b) The substrate illuminated by UV and the contact angle. A large amount of –OH groups are generated on the surface of oxide. The contact angle is getting smaller. (c) The substrate with assembled APTES monolayer. The contact angle is getting larger again indicating the presence of SAM layer. 32

Figure 2.7 (a) The SEM image of the sensor with the sensing material. (b) Magnified porous sensing material. 33

Figure 2.8 Setup of the gas sensing measurement system for wet CO_2 detection. ...36

Figure 2.9 Setup of the gas sensing measurement system for dry CO_2 detection. ...36

Figure 3.1. Double-sweep DC IV curve of the PVA sensor at 25ºC. 40

Figure 3.2. Sensing performance of the PVA sensor for 400-ppm CO_2 at 25ºC. 40

Figure 3.3. Degradation of the PVA CO_2 sensor after two weeks of storage in air. 41

Figure 3.4. The PVA sensor didn't respond to CO_2 gas after heated at 180ºC for 1 hour. 41

Figure 3.5. Water molecules bond with the −OH groups of PVA molecules and play a principal role in the detection of CO_2 (according to [33]). 42

Figure 3.6. Various types of CNT nanotubes [38]. 44

Figure 3.7. Double-sweep DC IV curves of the SWNT sensor and the PEI-SWNT sensor at room temperature. The I-V hysteresis of the PEI-SWNT sensor is smaller than that of the SWNT sensor. 44

Figure 3.8. Schematic of PEI-bonded CNT [40]. 45

Figure 3.9. Double-sweep PIV curves of the SWNT sensor (a) and the PEI-SWNT sensor (b) at 25ºC after programming. 49

Figure 3.10. Dry CO_2 sensing properties of the PEI-SWNT sensor measured by applying DC biases at 25ºC after one day (a) or two weeks (b) after the sensing material is deposited. 50

Figure 3.11. Wet CO_2 detection characteristics of the PEI-SWNT sensor measured by applying DC bias at 25ºC. 51

Figure 3.12. (a) Voltage pulse scheme for measuring sensing characteristics. (b) Wet CO_2 detection characteristics of the PEI-SWNT sensor measured by applying the voltage pulse at 25ºC. 52

Figure 3.13. I_D-V_{CGS} characteristics showing Na^+ ion-blocking capability of APTES SAM. Figures (a) and (b) show the I_D-V_{CGS} curves of the sensors with and without the APTES ion-blocking layer, respectively, as a parameter of measurement

temperature (20°C and 160°C). The insets plot the I_G-V_{CGS} curves showing the control-gate leakage current. 56

Figure 3.14. (a) The penetration of Na ions. (b) The protective effects of the APTES monolayer. 57

Figure 3.15. The $–NH_2$ functional groups capture Na^+ ions and form a complex of APTES-Na^+ to prevent the penetration of Na^+ ions. 58

Figure 3.16. I_D-V_{CGS} curves of three FET platforms having different materials (nothing (air), APTES SAM only, both APTES SAM and sensing material) on the exposed interdigitated FG and CG at measurement temperatures of 20ºC (a) and 160ºC (b). The insets are the I_G-V_{CGS} curves. 60

Figure 3.17. The chemical formulas of ODTS and F-OTS. The functional groups of ODTS and F-OTS are $–CH_3$, and $–CF_3$, respectively. 62

Figure 3.18. I-V curves of sensors with ODTS and F-OTS at 20ºC. Large leakage currents are found in both ODTS and F-OTS sensors. 62

Figure 3.19. CO_2 sensing performance of the proposed sensor with N_2 as the reference gas at 160ºC. The increase of CO_2 concentration induces the increase of the drain current $|I_D|$. 64

Figure 3.20. (a) The *I-V* curves of the sensor before and after programing. (b) I_D transient curve of the sensor in N_2 ambience after programing, which indicates stability of the sensor. 67

Figure 3.21. (a) Sensing performance of the programed sensor for 500 ppm CO_2 with N_2 reference gas at 150ºC. (b) ΔI_D as the function of CO_2 concentration after programming the sensor. $\Delta I_D=|I_{D\_G}|-|I_{D\_B}|$. 68

Figure 4.1. Related reactions and chemical species involved in the adsorption of CO_2 by PEI. The R, R', and R'' are either organic substituent of hydrogen atoms [57]. 74

Figure 4.2. The equivalent circuit of the sensor with PEI-SWNT. (a) The sensing material is simplified as a series connection of the R_{CG} and C_{CG}. The C_{pass}, C_{FG} and

C_p are the ONO passivation, floating gate, and parasitic capacitances, respectively. (b) shows the equivalent circuit of the sensor along A-A' in (a). The γ refers to the gate coupling coefficient between the FG and CG. 75

Figure 4.3. Schematic of the charge distribution within the sensor during the operation. 80

Figure 4.4. The equivalent circuit of the sensor with Na^+ ionic conducting material. (a) The sensing material is simplified as a series connection of the R_{bulk}, C_{sens} and C_i, which represents the resistance of sensing material bulk, the capacitance at the interface between sensing layer and CG, and the capacitance at the interface between sensing layer and the APTES monolayer. The C_{pass}, C_{FG} and C_p are the APTES-covered ONO, floating gate, and parasitic capacitances, respectively. (b) The equivalent circuit of the sensor from A to A' in (a). 81

List of Tables

Table 1.1. Various metal oxides for CO_2 detection and their working temperatures [11]–[16]. 10

Chapter 1
Introduction

1.1 Study background

1.1.1 Carbon dioxide monitoring and controlling

Carbon dioxide (CO_2) is a slightly toxic, colorless, and odorless gas with a slightly acid taste [1], [2]. It is a small but important constituent of the atmospheric air as it places an essential role in the Earth's carbon cycle. Nevertheless, CO_2 is also defined as a kind of greenhouse gases because it absorbs infrared light and can induce global climate change. The source of CO_2 in air can be classified into natural and human emissions. The natural sources include ocean-atmosphere exchange, plant and animal respiration, soil respiration and decomposition, and volcanic eruptions; the human sources include industrial processes, land use changes, and fossil fuel use [3]. Both the natural and human emissions can lead variations in the concentration of the atmospheric CO_2 over space and time. However, human activities make the main contribution to the rapid concentration increase especially

after the industrial revolution even though human CO_2 is a tiny component of total emissions [4]. Fig. 1.1 (a) and (b) present the atmospheric CO_2 concentration change over time recorded by Mauna Loa Observatory [5]. In Fig. 1.1 (a), the industrial revolution in the year of 1958 marked a major turning point of the CO_2 increasing rate. As shown in Fig. 1.1 (b), the concentration increased from about 315 ppm in 1958 to 407.28 ppm by November, 2018.

The monitoring of CO_2 outdoor by using gas sensors helps researchers to know the change in the quality of the atmospheric air and provides important data for environment research. In the field of indoor application, it is also necessary to develop reliable CO_2 sensors, especially home and office air qualities monitoring and controlling. A high CO_2 concentration indoor can trigger many symptoms for human, such as headaches, nausea and etc. Fig. 1.2 shows typical CO_2 levels and their effect on human beings [6]. A level of less than 1000 ppm is recommended, but if the concentration is higher than 5000 ppm, it could bring health risks. Recently, people increasingly expect portable and integratable sensors to make life more convenient. To meet the requirements for various application fields, numerous

sensing materials, device structures and mechanisms of CO_2 sensing have been investigated. So far, many kinds of CO_2 sensors have been developed by research groups all over the world. Based on the sensing mechanism, they can be divided into physical and chemical ones, and the chemical sensors includes the ones rely on chemical adsorption, and electrochemical reactions [7].

The most widely used physical CO_2 sensor relies on the optical sensing principle. Fig. 1.3 presents two typical nondispersive infrared (NDIR) CO_2 sensors [8], [9]. The NDIR sensor consists of a light source, a gas chamber and a light detector. The detector receives lights from the light source through the gas chamber. As CO_2 absorbs infrared radiation at specific wavelengths, when CO_2 gas diffuses into the chamber, the light intensity reaching to the detector decreases. In Fig. 1.3 (a), the light source and detector are located at both sides of the chamber. To achieve a high regulation and fine accuracy, the gas chamber needs to be extended to increase the effective path-length of the light, which results in a quite large size of the sensor. Therefore, a parabolic mini mirror is adapted for folded or multiple reflection of the light so that sensor size can be reduced as shown in Fig. 1.3 (b) and

(c). The optical sensors have low operating temperature, long lifetime and high sensing speed. But because of their sensing mechanism, it is difficult to reduce the size of the sensors and their optical components lead to the problem of high power consumption.

In the case of CO_2 sensors based on chemical adsorption, the sensors usually consist of two electrodes connected by various sensing materials to measure the resistance or capacitance changes of the sensing materials. As metal oxides have the advantages of low cost, simplicity of their use, and large number of detectable gases [10], they have been widely investigated to detect CO_2, for example, insulator oxides like Al_2O_3, p-type semiconducting oxides like Bi_2O_3, Cr_2O_3, n-type semiconducting oxides like SnO_2, TiO_2, and composite metal oxides like CeO_2-$BaCO_3$-CuO, and SnO_2-La_2O_3 [11]−[17]. Table 1.1 shows a variety of metal oxides for CO_2 detection and their working temperatures [11]–[16]. At their appropriate operating temperatures, CO_2 molecules adsorb on the surface of oxides and react with them resulting in the changes in resistance or capacitance of the sensing materials. However, as the bond angle of CO_2 molecules is 180º, it makes the

chemical properties of CO_2 very stable and noble, and requires high energy to support the sensing chemical reactions. Consequentially, the working temperature of this type of CO_2 sensor ranges from 300°C to 1000°C as listed in Table 1.1.

The final type is electrochemical CO_2 sensor. It can be divided into potentiometric sensor and amperometric sensor. Fig. 1.4 shows two examples of electrochemical CO_2 sensors [18], [19], where (a) is a potentiometric sensor and (b) is an amperometric sensor. The potentiometric sensor has a working electrode, a reference electrode and a solid electrolyte. On the reference electrode side of the sensor, there is a sealed air chamber, where the concentration of CO_2 will be zero or fixed at a certain level. On the working electrode side, the sensing material (sensing electrode) is exposed to target gases (CO_2 in air). With measuring the electromotive force (EMF) between the two electrodes, the change of CO_2 concentration associated with the change in EMF will be tracked. The amperometric sensor has two or three electrodes (there are two electrodes in the example of (b)). When a voltage is applied to those two electrodes, a current will flow through the electrolyte, which is measured and recorded as the sensing signal. As the

concentration of CO_2 changes, the equilibrium of the reversible electrochemical reactions at both two electrode sides will be broken and re-established. As a result, the measured current changes as a function of the CO_2 concentration. This type of sensor still requires high operating temperature (above 300°C). Moreover, they are usually discrete devices with large size and it is very difficult to integrate them with CMOS technology.

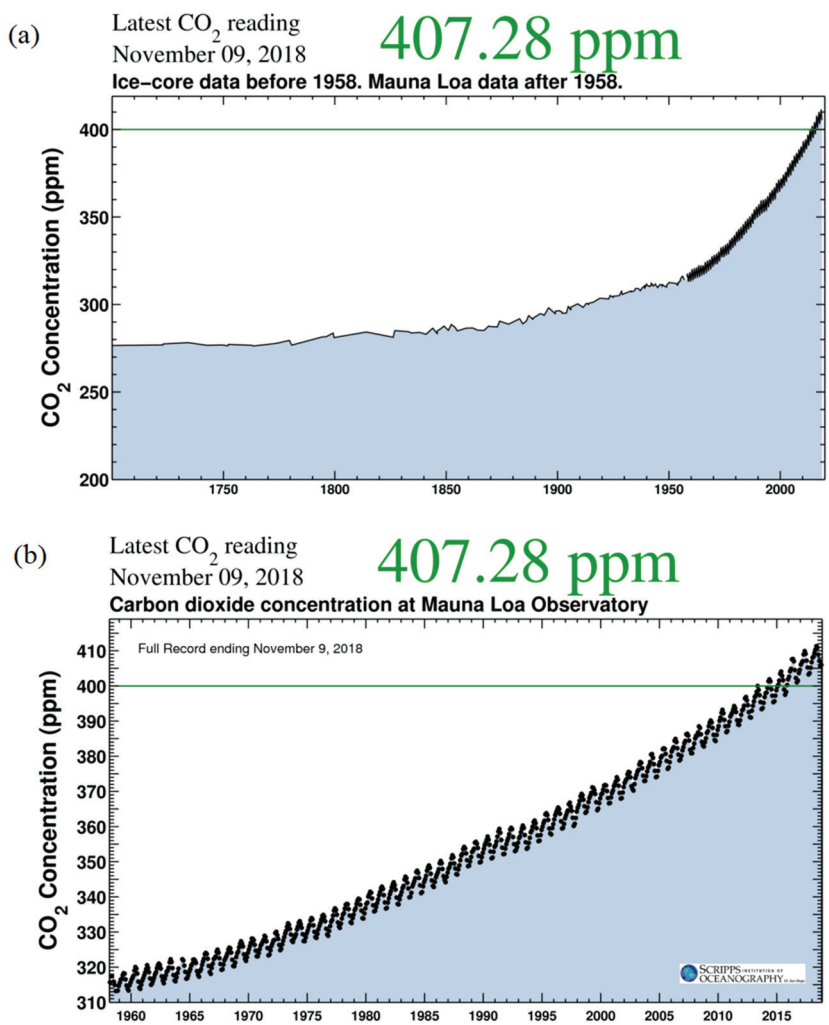

Fig. 1.1 Change in concentration of CO_2 in air over time [5]. (a) CO_2 concentration record from the year of 1700 to present. (b) CO_2 concentration record from 1958 to present.

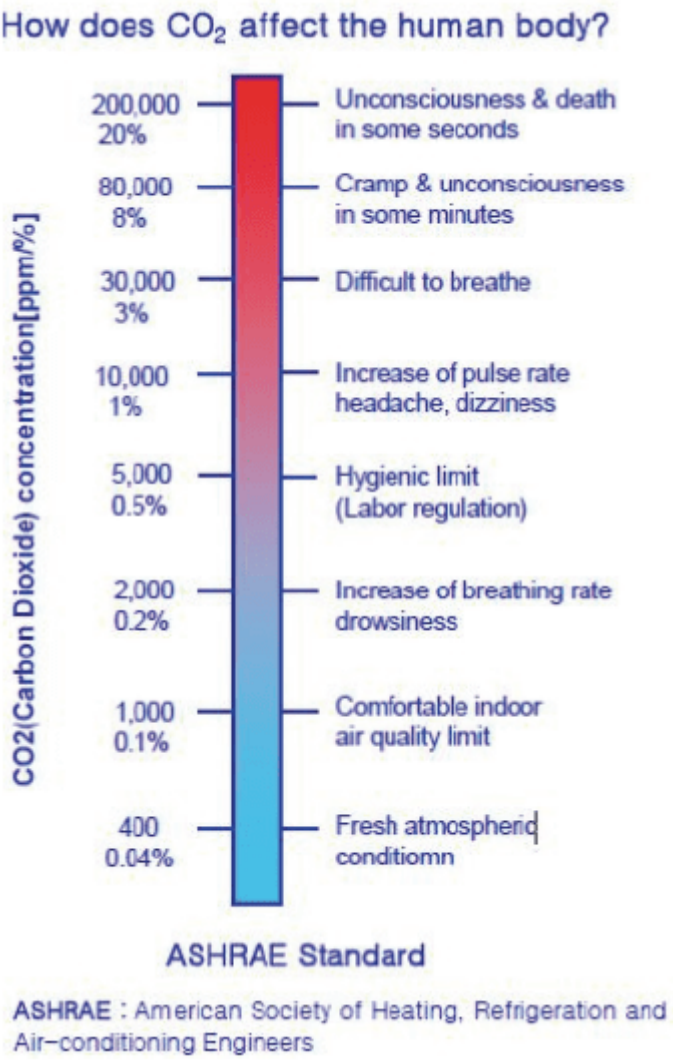

Fig 1.2 Typical CO_2 levels indoor and their effects on human beings [6].

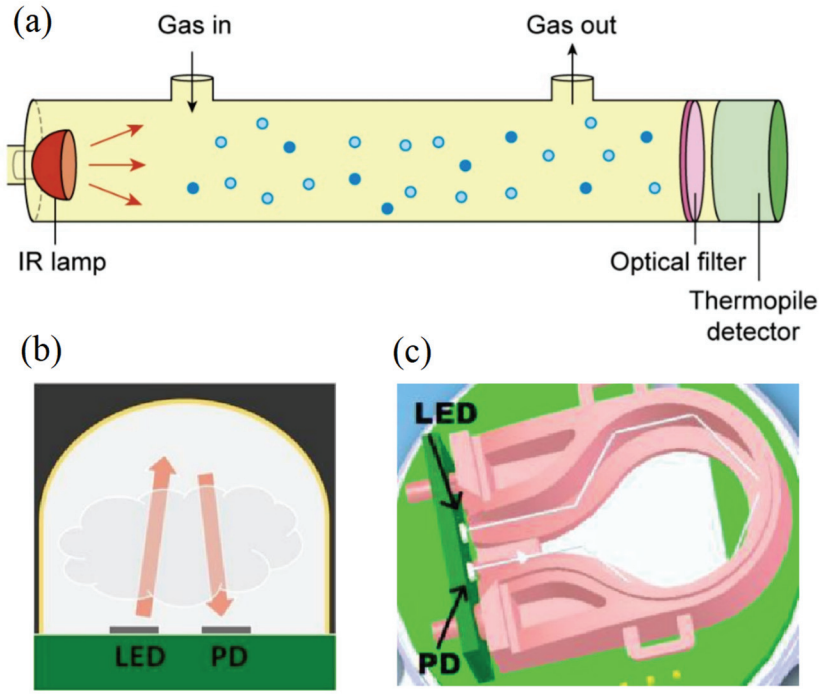

Fig. 1.3 The schematic diagram of optical CO_2 sensor with a straight light path (a) [8], a folded reflection (b) and a multiple reflection (c) [9]. The PD in the figure refers to the photodiode.

Sensing material	Classification	Working temperature	Reference
Al_2O_3	Insulator	450°C	[11]
Bi_2O_3	p-type semiconductor	450°C	[11]
Cr_2O_3	p-type semiconductor	450°C	[11]
CuO	p-type semiconductor	450°C	[11]
NiO	p-type semiconductor	450°C	[11]
CdO	n-type semiconductor	450°C	[11]
Fe_2O_3	n-type semiconductor	450°C	[11]
TiO_2	n-type semiconductor	450°C	[11]
ZnO	n-type semiconductor	450°C	[11]
SnO_2	n-type semiconductor	350°C	[12]
WO_3-loaded TiO_2	composite	600°C	[13]
$BaTiO_3$(CeO_2 /ZrO_2 /$CaCO_3$ /Nd_2O_3 /La_2O_3 /Fe_2O_3)	composite	300-640°C	[14]
CeO_2 with $BaCO_3$, CuO	composite	550-600°C	[15]
La-coated SnO_2	composite	400°C	[16]

Table 1.1. Various metal oxides for CO_2 detection and their working temperatures [11]–[16].

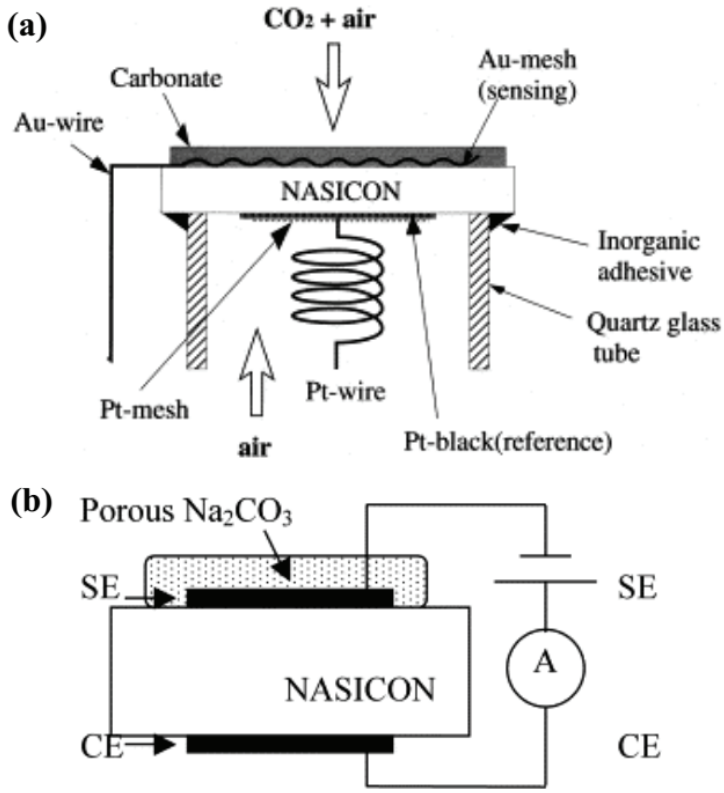

Fig. 1.4 Examples of electrochemical CO_2 sensors. (a) Potentiometric sensor [18].

(b) Amperometric sensor [19].

1.1.2 Gas sensors based on FET platforms

To achieve the full potential of sensing materials, different kinds of sensor platforms are designed, some of which have been discussed in the above section. Recently, there is an increasing interest in field-effect-transistor (FET)-type sensors because they can be fabricated with standard CMOS technology used to make integrated circuits [20]. In this case, it is possible to reduce the size of sensors, lower the power consumption, and fabricate sensors in a reproducible way [21]–[23].

In 1975, Lundström et al. proposed the first Pd-gate FET gas sensor for H_2 detection as shown in Fig. 1.5 [24], [25]. This type of sensor has a Pd sensing gate. During the detection of H_2 gas, the gas molecules are adsorbed and can decompose into atoms at the outside surface of Pd. Thanks to the small size of H atoms, they can penetrate through the Pd gate and reach to the interface between Pd and gate oxide. Those H atoms will form a dipole layer at the interface resulting in a change in the threshold voltage (V_{th}) of the FET shown as Fig. 1.5. The proposed Pd-gate sensor opened the wide applications of FET to the field of sensor platform. However, because its sensing behaviors require the size of target gas molecules small enough

to penetrate through the sensing gate, the usage of this type of sensor for other target gases were limited.

In order to greatly expand the number of gas species that can be detected by FET sensors, Janata proposed a FET sensor platform with an air gap named suspended gate (SG) FET shown as Fig. 1.6 [25], [26]. It has a suspended gate bonded to the substrate. An air gap is generated between the suspended gate and gate oxide. The sensing material is attached to the gate to absorb the target gas. As the capacitance between the gate and channel is changed by the target gas, the V_{th} is changed. The air gap allows gas molecules access to the sensing material regardless of the size. However, the gate oxide could be contaminated very easily, which will induce considerable noise and fluctuation of V_{th} and sensing signals. Therefore, a capacitively-controlled FET (CCFET) with a floating gate was proposed by researchers, which is shown in Fig. 1.7 [27]. The CCFET with a floating gate dramatically improves the sensing performance of sensors, but it complexed the fabrication of sensors to cover the suspended gate with sensing material and bond the gate to the substrates. To simplify the fabrication process and

make the device more compatible with standard CMOS technology, our group proposed a FET sensor platform having horizontal floating gate and control gate. Fig 1.8 shows the sensor with horizontal floating gate and control gate investigated in our previous work [28]. The platform was fabricated with standard CMOS technology. The sensing material was formed at the final step after the fabrication of the platform.

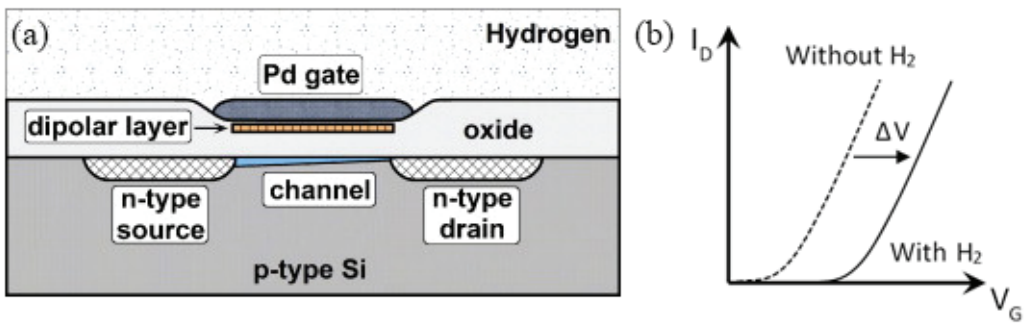

Fig. 1.5 Lundström FET H_2 sensor. (a) Shematic of the sensor [25]. (b) The V_{th} of the FET is changed by H_2 gas.

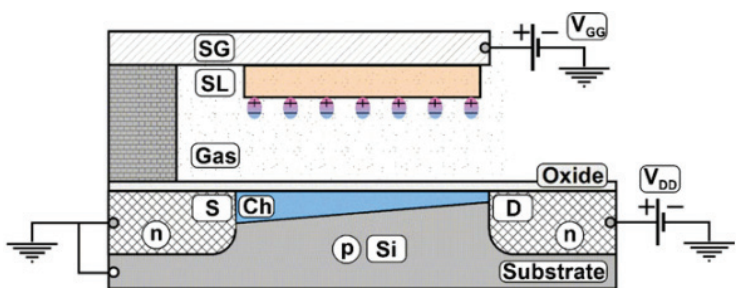

Fig. 1.6 Suspended gate (SG) FET sensor with an air gap [25].

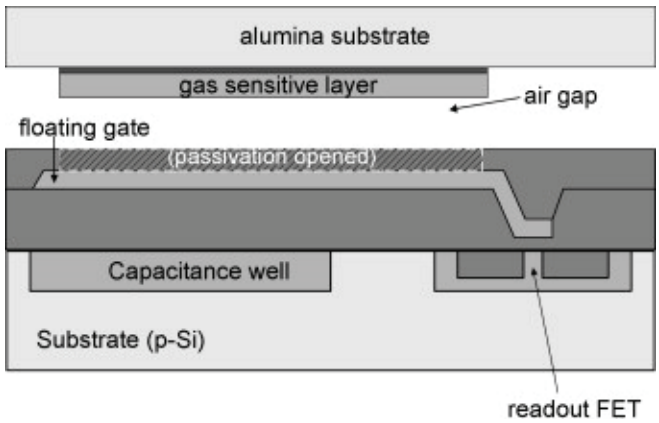

Fig. 1.7 Capacitively-controlled (CC) FET sensor with a floating gate [27].

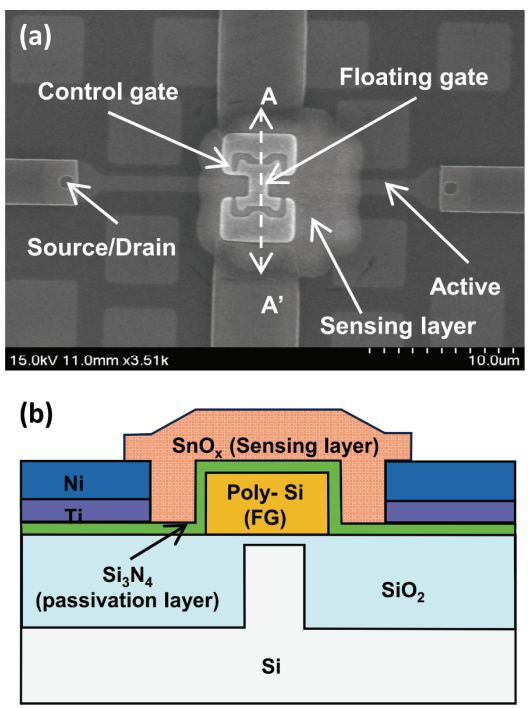

Fig. 1.8 FET sensor platform having a horizontal floating gate and control gate [28].

(a) The SEM image of the sensor. (b) The cross sectional view cut along line A-A'

in (a).

1.2 Purpose of research

Even though a lot of efforts have been made to lower the working temperature of the chemical and electrochemical CO_2 sensors, further more research is still required for achieving a stable FET CO_2 sensor having low power consumption and low working temperature. In this work, we combined various novel sensing materials with FET platform for CO_2 detection to reduce the working temperature. Carbon based sensing material and PVA polymer are able to detect CO_2 at room temperature. Whereas, the sensing mechanism seriously relays on the help of moisture (water vapor), which limits the application of the sensor. Finally, a sodium ionic conducting materials is applied to the platform. As known that sodium ions have high mobility and can induce unacceptable instabilities in MOSFET operation, so they should be avoided in CMOS technology. If the ions inside the sensing material penetrate into the FET platform, they will cause serious problem of stability of the sensor. Fortunately, with the protection of a self-assembled monolayer – APTES, sodium ions can be prevented from leaking into the substrate.

1.3 Dissertation outline

In this work, CO_2 sensors based on FET type platform with horizontal floating gate and control gate working at low temperature are proposed and investigated. Chapter 2 introduces the detailed fabrication flow of the FET platform and the formation of sensing materials. Chapter 3 shows the measurement results and discussion about the electrical and CO_2 sensing properties of the sensors with various sensing materials. In Chapter 4, the sensing mechanisms of the sensors with the carbon based material and the sodium ionic conducting material are explained and modeled. Finally, Chapter 5 concludes this work with a summary.

Chapter 2

Device structure and fabrication

2.1 FET platform structure and fabrication

The FET platform used in this work is shown in Fig. 2.1. Fig. 2.1 (a) is the SEM top view of sensor platform, (b) and (c) are the schematic cross sectional views cut along A-A' and B-B' in (a), respectively. As shown in Fig. 2.1, the floating gate (FG) and control gate (CG) are formed horizontally. An interdigitated pattern is adopted to guarantee a promising coupling ratio between the two gates. Note that, an SU-8 passivation layer covers the whole substrate except the FG-CG area (marked out in Fig. 2.1 (a)) and electrode contact pads. Because the sensing material will be deposited in the final step, the SU-8 protects the active regions of FET from unwanted contaminations and only expose the interdigitated FG-CG region to the sensing material. To fabricate the FET substrate, 5 masks are needed. The main process flow is shown in Fig. 2.2.

The process starts with a 6-inch n-type (100) Si water. Firstly, the wafer is

cleaned using RCA cleaning process to remove oxides and all particles on the wafer. After cleaning, 10-nm SiO_2 and 150-nm Si_3N_4 are formed through dry oxidation and low pressure chemical vapor deposition (LPCVD) processes, respectively. With the first mask, the active device regions are defined by photolithography process. The silicon substrate with Si_3N_4/SiO_2 mask patterned by dry etching shown as Fig. 2.2 (a). Through 2-hour wet oxidation, a thick field oxide with a thickness of about 550 nm is grown to insulate transistors (Fig. 2.2 (b)). Because Si_3N_4 is resistant to oxidation, thick oxide only grows within the regions without Si_3N_4, which is called as Local Oxidation of Silicon (LOCOS) process. Then the SiO_2/Si_3N_4 mask is removed by wet etching (H_3PO_4 for Si_3N_4 and HF for SiO_2) During LOCOS process, the Si_3N_4 could be oxidized by H_2O and generates NH_3 gas. The NH_3 gas can diffuse to the interface of Si and SiO_2, reacts with Si and produces Si_3N_4, so called white ribbon [29]. To remove the white ribbon, a 35-nm-thick oxide is grown by dry oxidation process, and a back-etch is conducted leaving 10nm oxide (sacrificial oxide) above the active regions. Then a punch-though and a buried channel implantations are processed. After removing the sacrificial oxide

by HF solution, a 10-nm-thick SiO_2 is produced by dry oxidation to serve as the gate oxide. A 200-nm-thick in-situ phosphorous doped Poly-Si layer is deposited and pattern using the second mask to form the FG. Stacked ONO insulator layers consisting of SiO_2 (10 nm) / Si_3N_4 (20 nm) /SiO_2 (10 nm) cover the whole substrate to prevent contamination of the platform from the final deposition step of the sensing material and the penetration of moisture after fabricating the device. The first layer of SiO_2 is thermally grown on the wafer, and the Si_3N_4 and the second SiO_2 are deposited by LPCVD and methanol to olefins (MTO) processes. Then the source and drain are implanted. To form the contact hole, the third mask is used, followed by the electrode metal deposition and lift-off process (Fig. 2.2 (c)). After defining the contact holes, stacked layers of Ti (20 nm) / TiN (30 nm)/ Au (30 nm) are formed consecutively by sputtering to serve as the CG, source, and drain electrodes. The electrodes are patterned by using the forth mask and this step is shown in Fig. 2.2 (d). The final step of FET substrate fabrication is SU-8 passivation layer deposition. In this step, a thick layer of SU-8 is deposited and patterned by spin coating and photolithography (Fig. 2.2 (e)). In this way, only the FG-CG area

(marked in Fig. 2.1 (a)) and electrode contact pads are exposed to the air. Fig. 2.2 (f) shows the FET substrate covered by sensing material. Finally, several sensing materials are deposited on the fabricated substrate and are investigated for CO_2 detection at relative low temperature in this work.

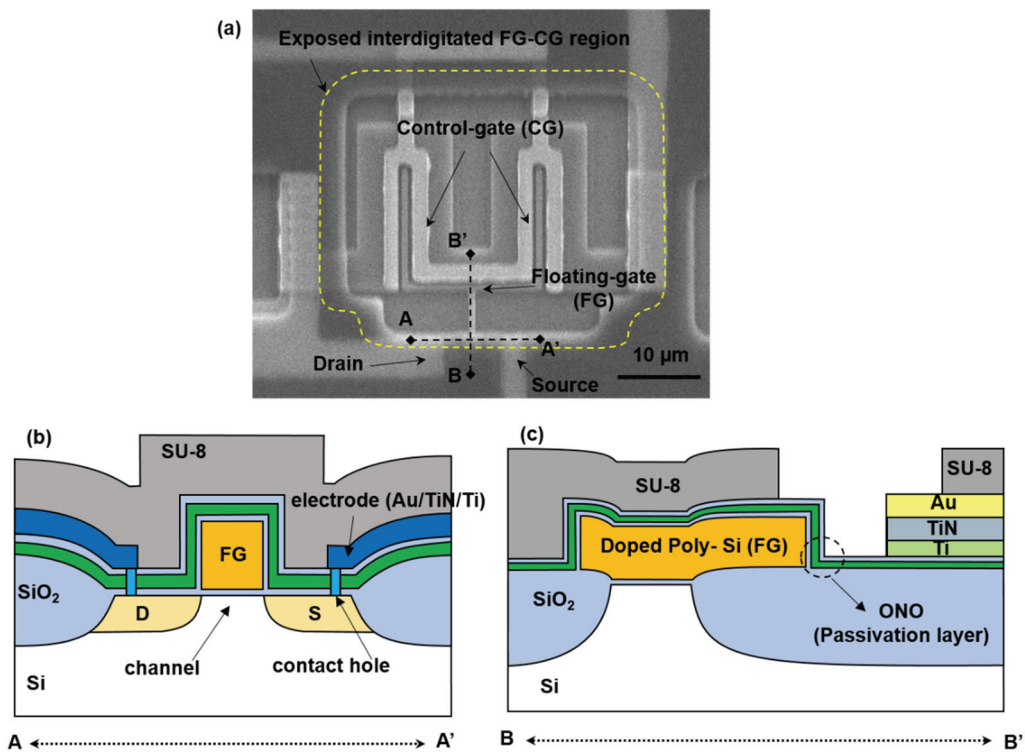

Fig. 2.1. (a) SEM top view of sensor platform. (b) Schematic cross sectional view cut along A-A'. (c) Schematic cross sectional view cut along B-B'.

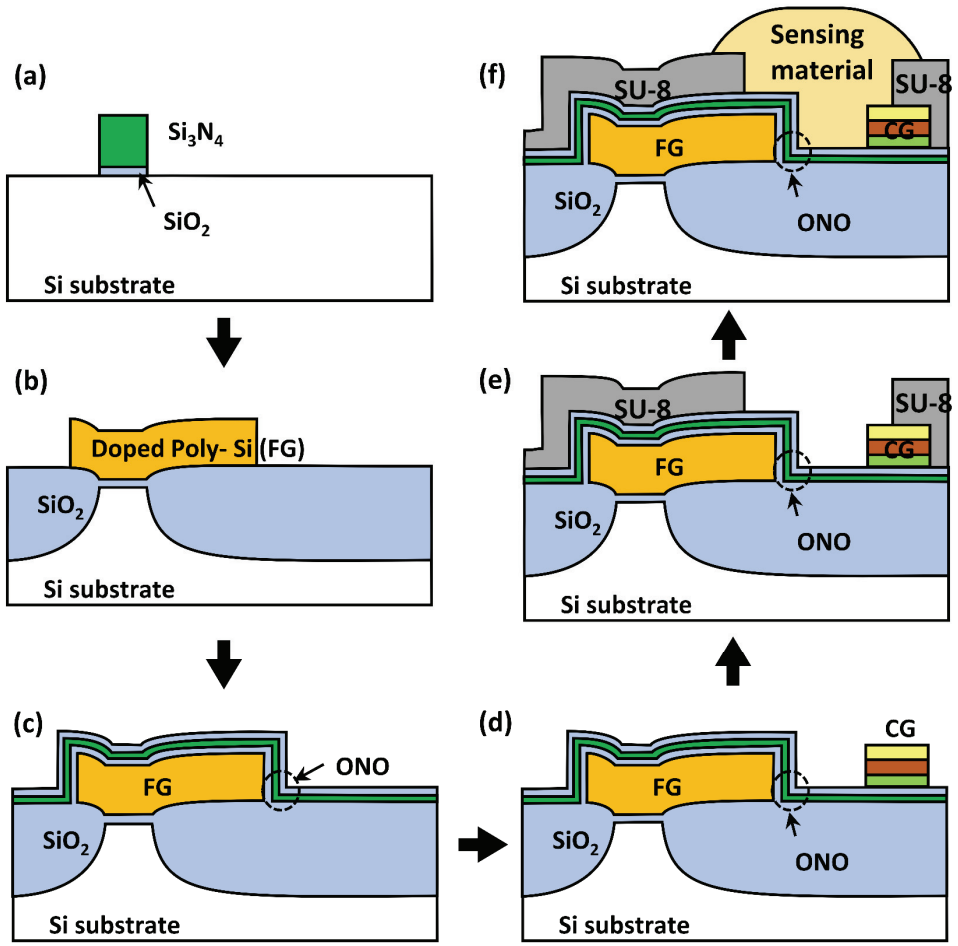

Fig. 2.2 The main fabrication flow of the FET substrate. (a) Silicon wafer with patterned Si_3N_4/SiO_2. (b) The FG is patterned. (c) ONO stack is deposited to cover the whole substrate. (d) Electrodes are patterned. (e) The SU-8 layer is deposited and patterned to expose the interdigitated FG-CG and electrode pads only. (f) The sensor with sensing material.

2.2 Sensing materials deposition

In this work, all the sensing materials were deposited on the sensor FET substrates by inkjet printing process. The instrument for inkjet printing used in this work is Omni Jet 100. To reduce the working temperature of the CO_2 sensor, various kinds of sensing materials were investigated in this dissertation, including organic polymers, carbon based nanomaterials, and inorganic ionic conducting materials. The following sections will provide introduction to the sensing materials used in this work and their deposition processes.

2.2.1 Organic polymer based sensing material

Polymer materials have attracted increasing attentions recently because they can be fabricated by low-cost and simple processes, and require low gas sensing temperature. In this work, Polyvinyl alcohol (PVA) is used to detect CO_2, based on the reactions between CO_2 and –OH (with the help of water) at room temperature (25ºC). The PVA powders with an average mole weight (M_W) of 13000-23000 are purchased from Sigma-Aldrich (USA). As PVA is soluble in hot water, 0.2 g of purchased PVA powders is dissolved in 30 mL of mixture of deionized (DI) water

and DMOS (4:1 in volume). To make an appropriate ink solution, firstly, PVA powders are soaked in the solvent at 25ºC with stirring for 1h by using Hotplate & Magnetic stirrers (MTOPS production). In this process, the white particles turn into transparent. After that, the solid-liquid mixture is allowed to stand for 12 hours at 25ºC (swelling). Then we increase the temperature to 95 ºC and stir the mixture for 14 hours at 95ºC for sufficiently solving PVA particles. Finally, the solution is cooled at 25ºC, and filtered with 0.2 μm syringe filter. The chemical formula of PVA and the finally obtained ink solution is shown in Fig. 2.3. The as-prepared PVA ink is injected into 4 mL ink cartridge for printing. Fig. 2.4 (a) shows the PVA ink printed on the surface of FET sensor substrate at 25ºC and Fig. 2.4 (b) is the capture of ink droplet. After printing, the sensor is cooled in air for 12 hours and stored for measurement.

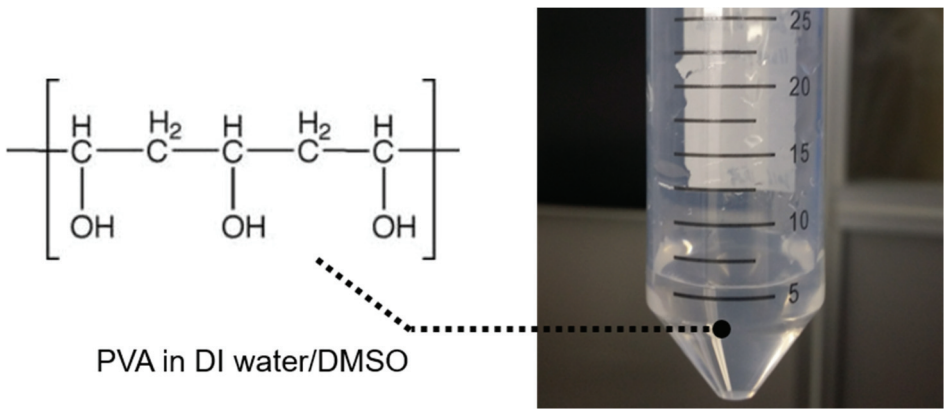

Fig. 2.3 PVA ink obtained by dissolving PVA powders in the mixture of DI water and DMOS (4:1 in volume).

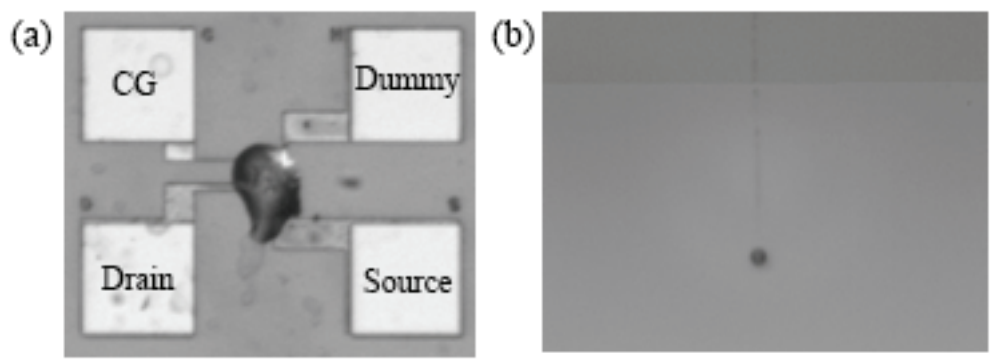

Fig. 2.4. (a) Printed PVA ink on the FET sensor substrate. (b) Capture of the ink flow printed from the ink cartridge.

2.2.2 Carbon based sensing material

Besides polymers, carbon based sensing materials, like CNT and graphene, have also attracted many attentions because they can detect CO_2 even at room temperature [30]. In this section, a sensing material of polyethylenimine (PEI) coated single-walled carbon nanotubes (SWNTs) is investigated for the detection of CO_2 at room temperature (25ºC). The layer-by-layer PEI-coated SWNT (PEI-SWNT) sensing materials are formed by inkjet printing.

Semiconducting SWNT ink (1mg 98%) is purchased from NanoIntrgris (Canada) and printed on the platforms at 50ºC without further processing. Then the device is annealed under vacuum at 250ºC for 3 hours to evaporate the solvent. The next step is to print the PEI to cover the SWNT random networks. Since ink having a viscosity of 1 to 10 cps is suitable for inkjet printing [31], when producing PEI ink, a Wt. 50% branched PEI aqueous solution (number average molecular weight 1200) purchased from Sigma-Aldrich (USA) is diluted to 10^{-3} mol/L with DI water to reduce the viscosity of the solution. After printing the PEI, the sensor is heated at 60ºC for 2 hours and then cooled in air for 1 hour. Fig. 2.5 presents the

microscopic images and schematics of the printed sensing materials. Fig. 2.5 (a) shows the platform used for the sensors having carbon based sensing materials. Fig. 2.5 (b) and (c) show the images of printed pure SWNT random network and PEI-SWNT, respectively. Coffee ring effect is rarely observed in the images indicating the printing condition of the SWNTs is reasonable. Unlike the pure SWNTs which concentrate densely in the center of the printed layer, the PEI molecules disperse the nanotubes and make their distribution more uniform. Fig. 2.5 (e) and (f) show the schematic 2D cross sectional view of the sensor with pure SNWT and PEI-SWNT cut alone line A-A' in Fig. 2.5 (a) which explaining how the PEI disperses the nanotubes.

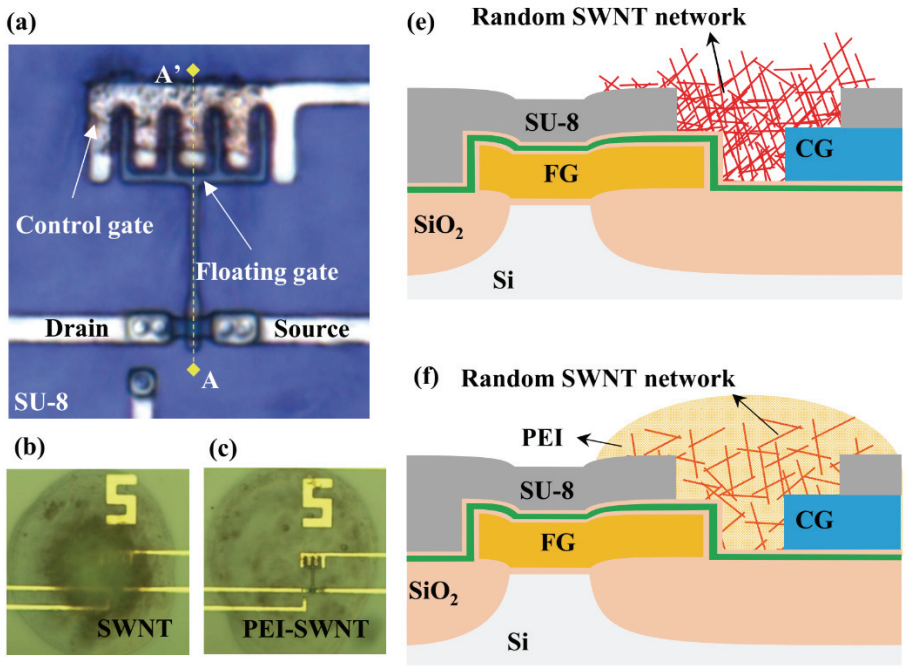

Fig. 2.5. (a) the platform used for the sensors having carbon based sensing materials. (b) and (c) show the images of printed pure SWNT random network and PEI-SWNT. (e) and (f) show the schematic 2D cross sectional view of the sensors with pure SNWT and PEI-SWNT cut alone line A-A' in (a), illustrating the dispersion of the nanotubes by PEI.

2.2.3 Sodium ionic conducting sensing material

Alkali carbonates and related ionic conducting materials are widely used in the field of CO_2 detection based on electrochemistry, especially materials containing sodium ions. However, it is required to avoid mobile ions like Na^+ ions as much as possible in the CMOS fabrication. As a result, most of the electrochemical CO_2 sensors are discrete devices and other planar ones are usually formed on insulate substrate (like, Al_2O_3 substrate). In this work, a sensing material full of Na^+ ions, the compound of Na_2CO_3 and $NaNO_2$, are applied for CO_2 detection. Experiment shows if the sensing material is directly deposited on the surface of the FET sensor substrate, the Na^+ ions inside the sensing material will penetrate very easily into the oxide and induce large leakage currents. Therefore, before the deposition of the sensing layer, a self-assembled monolayer (SAM) of (3-Aminopropyl) triethoxysilane (APTES), of which the linear formula is $H_2N(CH_2)_3Si(OC_2H_5)_3$, is formed on the exposed interdigitated FG and CG region by using simple dipping method. The measurement results indicated that it can effectively prevent the Na^+ ions from diffusing through the insulator stack and even the thick isolation oxide.

Fig. 2.6 shows the process flow of forming the SAM layer. To conform the assembling of APTES on the substrate, the contact angles after each steps were recorded and presented in Fig. 2.6. Fig. 2.6 (a) left illustrates the initial substrate (covered by SiO_2) and the water contact angle. Firstly, the platform is illuminated by UV to create a large amount of –OH groups on the oxide in the exposed region of interdigitated FG and CG as shown in Fig. 2.6 (b). Because the –OH is more hydrophilic than SiO_2, the contact angle in the right side of Fig. 2.6 (b) is getting much smaller and close to zero compared to that in (a). Then the substrate is immersed in 1% APETS solution (dissolved in 99.99% Ethanol) for 30min. After baking at 120 ºC for 10min, the APTES monolayer assembles itself on the oxide surface of the ONO stack in the FET platform as shown in Fig. 2.6 (c). The contact angle is found to get larger again, which certifies that the APTES layer successfully assembles on the substrate.

For preparing the ink of sensing material, powders of Na_2CO_3 and $NaNO_2$ with a molar ratio of 1:3 were dissolved in DI water. Both chemicals were purchased from Sigma-Aldrich (USA) without further purification. After inkjet printing, a 2-

hour annealing process at 170ºC under vacuum condition was conducted to fully evaporate the water in the printed ink and form the porous Na_2CO_3 and $NaNO_2$ sensing layer (an average pore size of about 500 nm). Fig. 2.7 (a) shows the SEM image of the sensor with the sensing material and (b) shows the magnified porous sensing material.

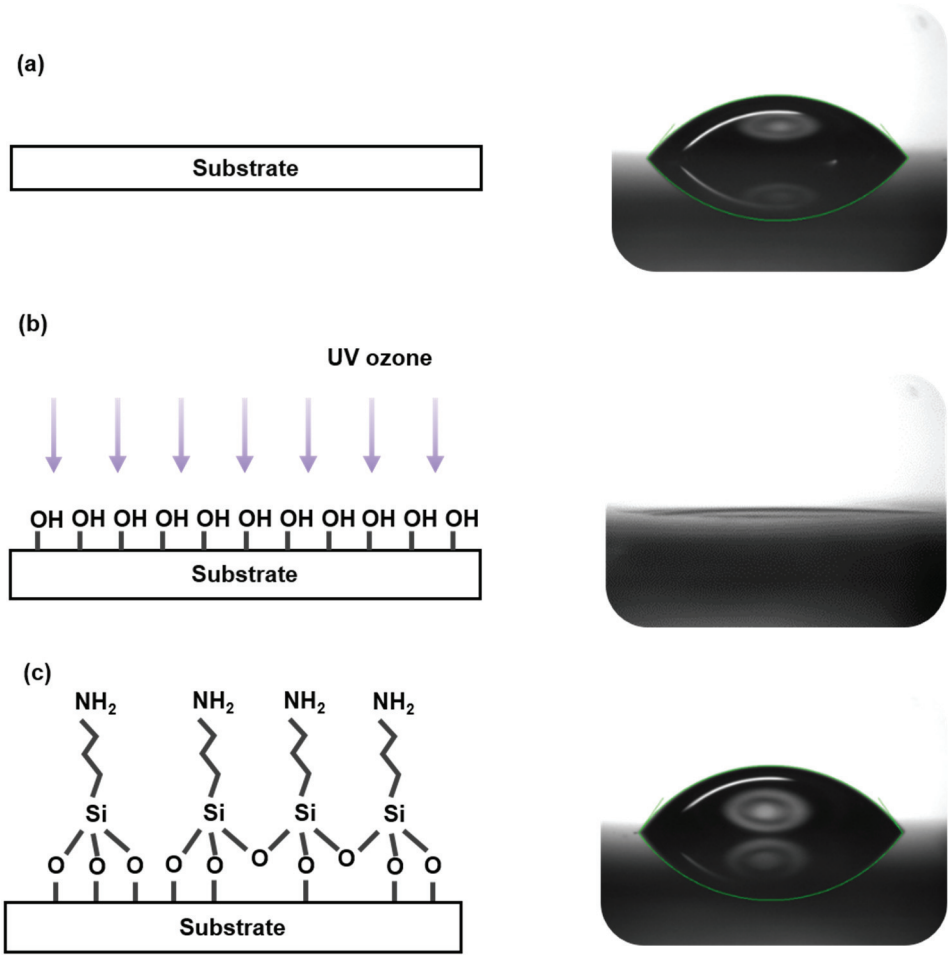

Fig. 2.6. (a) The initial substrate (SiO_2 covered silicon substrate) and its water contact angle. (b) The substrate illuminated by UV and the contact angle. A large amount of –OH groups are generated on the surface of oxide. The contact angle is getting smaller. (c) The substrate with assembled APTES monolayer. The contact angle is getting larger again indicating the presence of SAM layer.

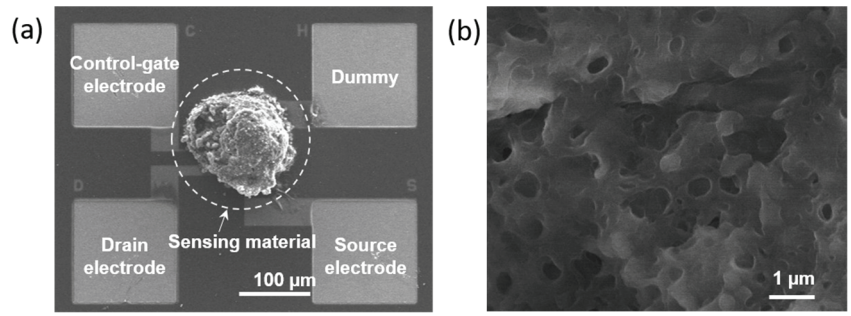

Fig. 2.7 (a) The SEM image of the sensor with the sensing material. (b) Magnified porous sensing material.

2.3 Gas sensing measurement system

Experiment found that water vapor plays a very important role when using PVA and PEI-SWNT to detect CO_2 at 25ºC (will be explained in Chapter 3 in detail). Thus both dry and wet CO_2 detection are investigated for them. In the measurement of sensors with Na^+ ionic conducting material, only dry gases are used. As discussed in literature [32], ambient water vapor may affect the detection of CO_2 by forming additional CO_3^{2-} and/or HCO_3^-. Because the working temperature of this sensor is kept around 160ºC, only the study of dry CO_2 sensing is focused on. For wet CO_2 detection, a bubbler is involved in the gas sensing measurement system, which is illustrated in Fig. 2.8. The MFC in the figure refers to the mass flow controller. The CO_2 gas samples are prepared by mixing 2000-ppm CO_2 diluted in N_2 with dry synthetic air (20 vol. % of O_2 and 80 vol. % of N_2). Reference gas 1 will flow through the bubbler to bring water vapor into the mixing chamber. By controlling the flow of reference gas 1, the relative humidity (RH) can be tuned. With fixing the total flow of reference gas1, reference gas 2 and CO_2 gas, the concentration of CO_2 and the RH level can be regulated well by changing the flow of these three

gases. Fig 2.9 shows the gas sensing measurement setup for dry CO_2 detection. The sensing characteristics are tested by switching between the sample target gas and the reference gas (dry air or pure N_2). Electrical measurements are carried out by using an Agilent B1500A including Waveform Generator/Fast Measurement Unit (WGFMU) pulse measurement module.

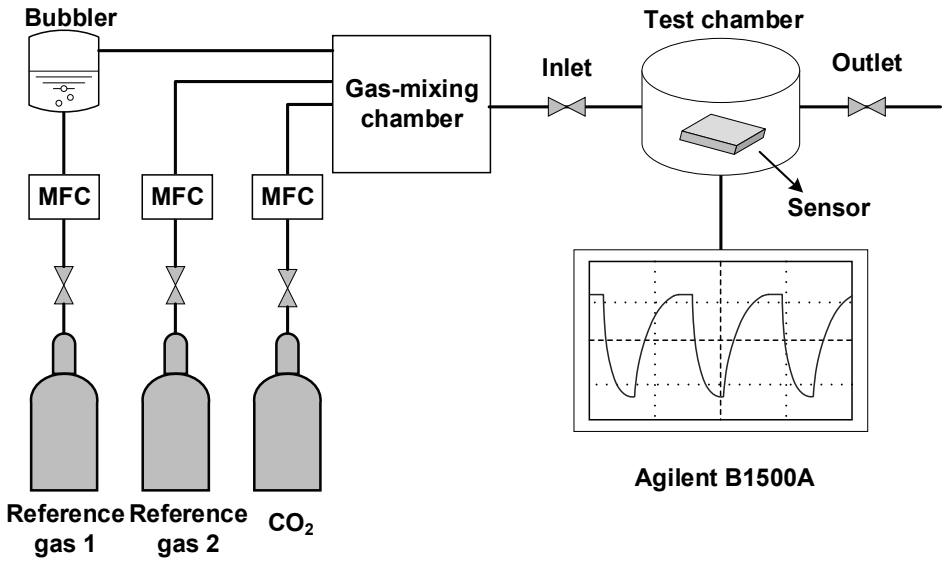

Fig. 2.8 Setup of the gas sensing measurement system for wet CO_2 detection.

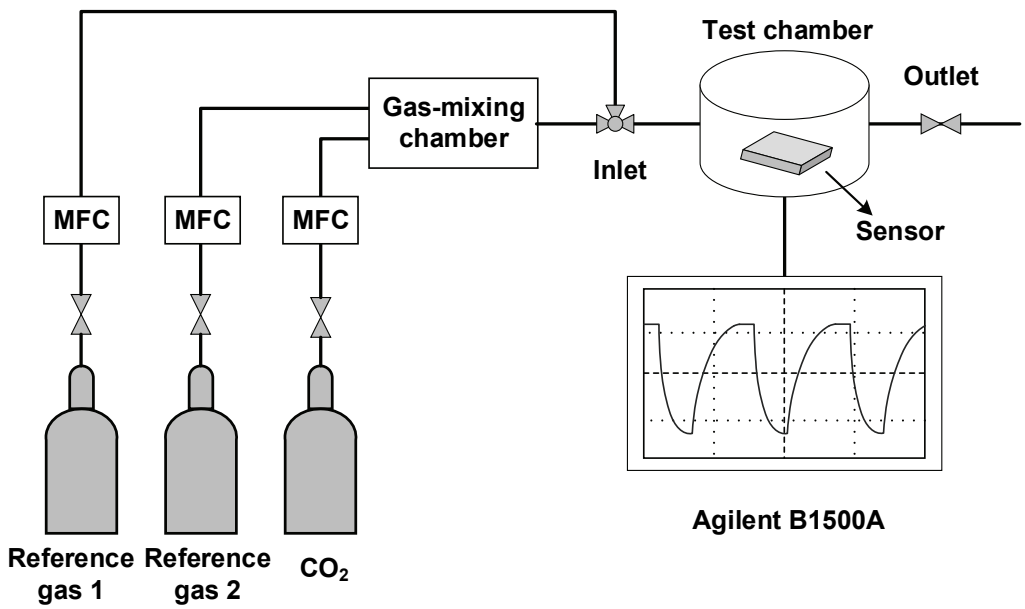

Fig. 2.9 Setup of the gas sensing measurement system for dry CO_2 detection.

Chapter 3

Measurement results

3.1 PVA CO_2 sensor

In this section, the basic electrical and CO_2 sensing characteristics of the PVA sensor are investigated at 25ºC. Fig. 3.1 plots the DC IV curve of the PVA sensor. Fig. 3.2 shows the sensing performance of the sensor for 400 ppm CO_2 at 25°C. As 400 ppm of CO_2 gas sample blows into the sensor for 5 min, the absolute drain current $|I_D|$ of the sensor decreases, and when the reference gas replaces CO_2 gas, the $|I_D|$ increases. The response of the sensor to CO_2 gas is defined as

$$response = \left[\left(\left|I_{D\_B}\right| - \left|I_{D\_G}\right|\right)/\left|I_{D\_B}\right|\right] \times 100\% \quad (1)$$

where I_{D_B} and I_{D_G} represent the drain currents of the sensor exposed to the reference gas and the target gas mixture, respectively. We define the response time (t_{RES}) as the rise time of $|I_D|$ to 90% of its maximum value, and the recovery time (t_{REC}) as the fall time to 10% of the difference between the maximum and reference currents. After calculation, the *response*, t_{RES}, and t_{REC} of the PVA sensor are 6%,

80 s and 60 s, respectively, for 400 ppm of CO_2 at 25°C.

Next, the PVA sensor is stored in air for two weeks, and the sensing performance is measured again as shown in Fig. 3.3. The measurement condition is the same with that of Fig. 3.2. During the response period, 400 ppm of CO_2 blows into sensor for 5 min and then reference gas replaces the CO_2 gas sample to refresh the sensor. It is obvious that the sensor cannot reach saturation current within 5 min. Moreover, the fluctuation of the drain current is getting larger compared to that of the results in Fig. 3.2. It illustrates that the sensor is degraded during storage in air.

To figure out the reason for the degradation, the sensor was heated at 180°C for 1 hour and then the sensing properties of the sensor for 400 ppm of CO_2 was measured again and shown in Fig. 3.4. This time, the sensor didn't respond to CO_2 any more. The reason seems to be that the water inside the PVA sensing material was fully evaporated after the 1-hour heating treatment. During the formation of the PVA sensing material, the device was just cooled and dried in air at room temperature. As the PVA ink for printing is composed of PVA, DI water and DMSO, water molecules may partially remain inside the sensing material even though the

DMSO is very easy to evaporate. According to literature [33], [34], water molecules bonds to the −OH groups of PVA through hydrogen bonding. These water molecules will react with CO_2 and induces the change in threshold voltage resulting in the decreases of the drain current. This process is illustrated in Fig. 3.5. It indicates that the water plays a principal role in the detection of CO_2 at room temperature when using PVA as the sensing material. Then wet air is used to blow into the sensor for 3 h and the CO_2 sensing performance was measured again. There was still no response of the sensor to CO_2 gas sample. According to literature [35]–[37], PVA can be decomposed by raising up the temperature and generate the production of water. In conclusion, the PVA sensor requires water vapor during the CO_2 detection at room temperature and has short life time, which limits its practical application in gas detection.

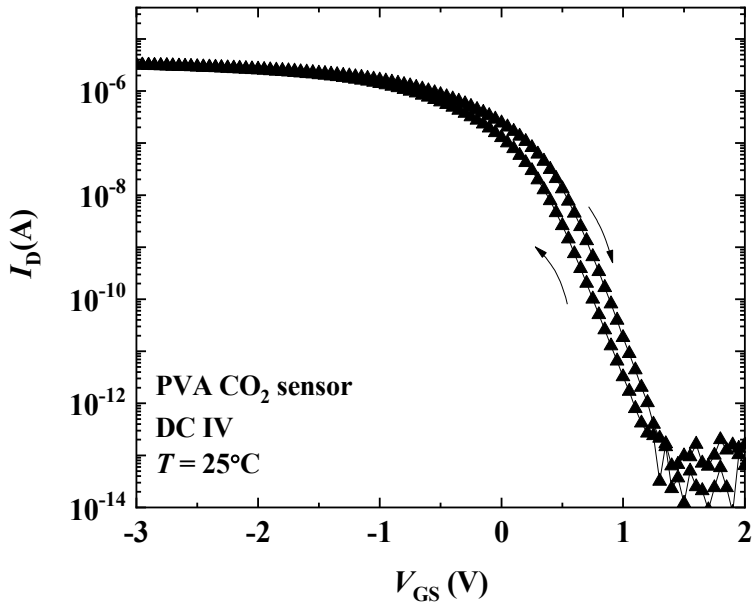

Fig. 3.1 Double-sweep DC IV curve of the PVA sensor at 25°C.

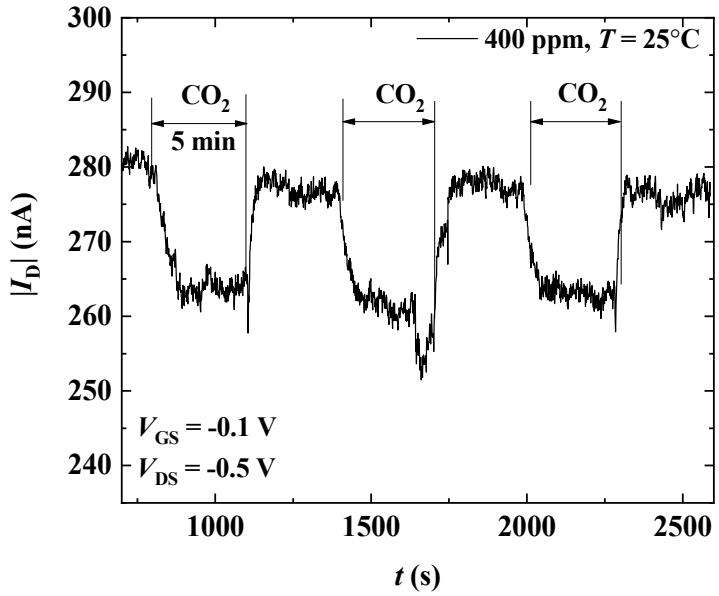

Fig. 3.2 Sensing performance of the PVA sensor for 400-ppm CO_2 at 25°C.

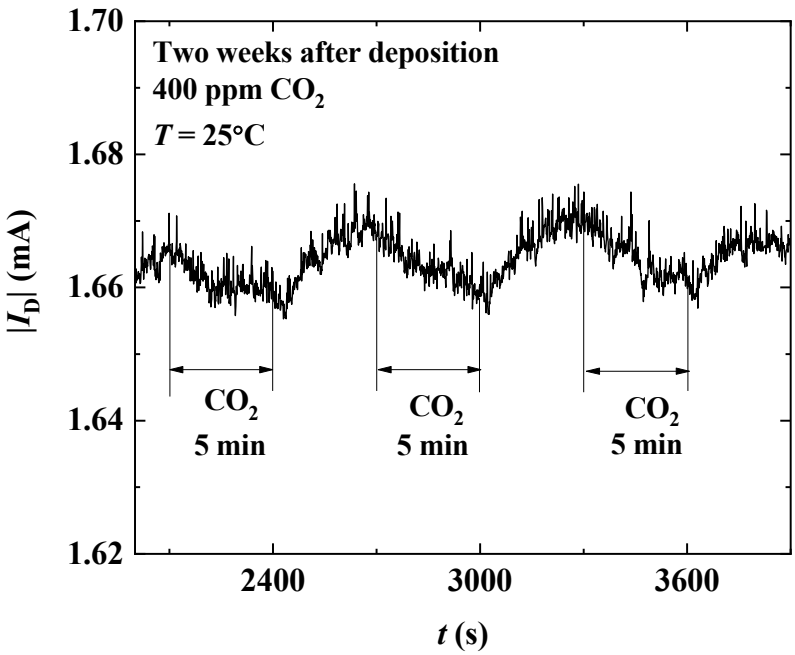

Fig. 3.3 Degradation of the PVA CO_2 sensor after two weeks of storage in air.

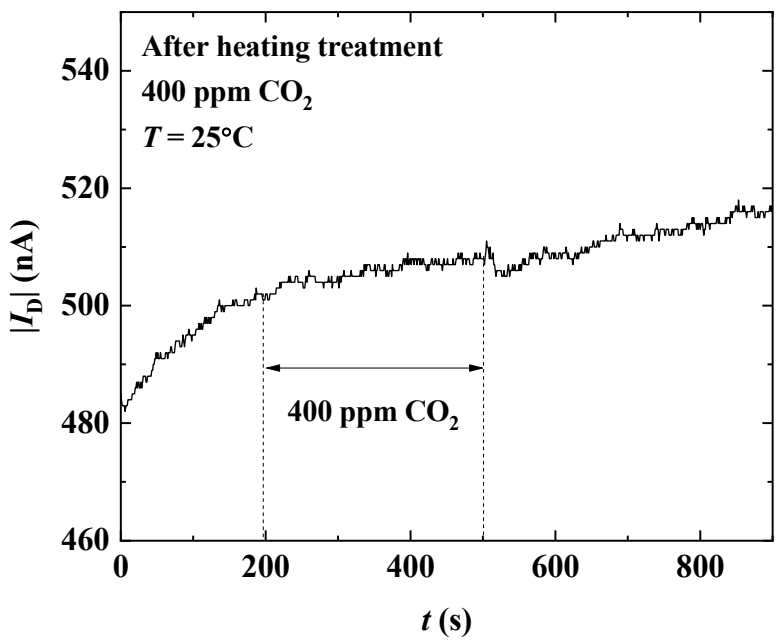

Fig. 3.4 The PVA sensor didn't respond to CO_2 gas after heated at 180°C for 1 hour.

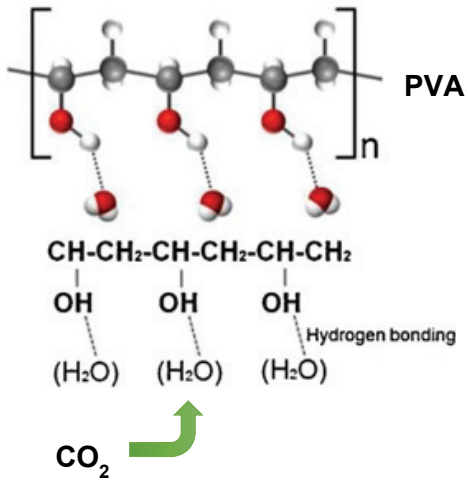

Fig.3.5 Water molecules bond with the −OH groups of PVA molecules and play a principal role in the detection of CO_2 (according to [33]).

3.2 PEI-SWNT CO_2 sensor

In this section, PEI coated SWNT sensing material is used for CO_2 detection at 25ºC. SWNTs have different conducting types depending on their lattice structures as shown in Fig. 3.6 [38]. In this work, p-type semiconducting SWNT is used. Branched PEI covers the SWNT for reducing the hysteresis.

Fig. 3.7 shows double-sweep DC IV curves of the SWNT sensor and the PEI-SWNT sensor at 25ºC. By comparison, the PEI-SWNT sensor has much smaller I-V hysteresis than the SWNT sensor with the help of PEI coating. According to literature [39], as the SWNTs contact silicon dioxide, a large amount of traps will be generated at the interface and induce a significant I-V hysteresis due to charge trapping and detrapping. Whereas, by coating the SWNT with PEI, the nanotubes will be dispersed by PEI. The schematic of PEI-bonded CNT is shown in Fig. 3.8 [40]. The PEI coating reduces the contact of SWNT network with the oxide, resulting in less interface traps. Therefore, the hysteresis is reduced.

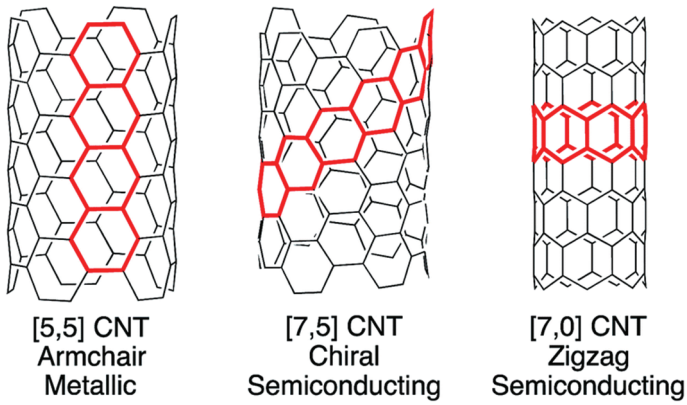

Fig. 3.6 Various types of CNT nanotubes [38].

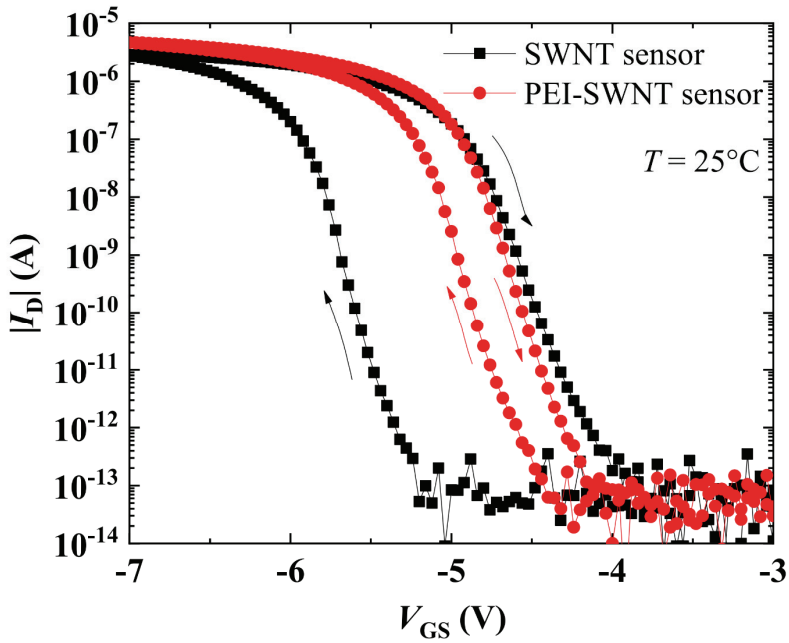

Fig. 3.7 Double-sweep DC IV curves of the SWNT sensor and the PEI-SWNT sensor at room temperature. The I-V hysteresis of the PEI-SWNT sensor is smaller than that of the SWNT sensor.

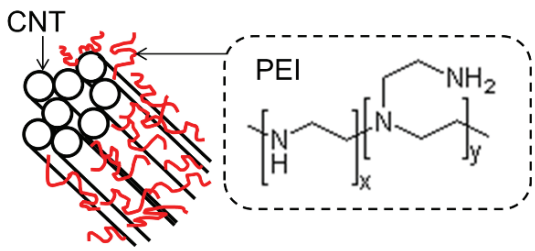

Fig. 3.8 Schematic of PEI-bonded CNT [40].

The FET sensor substrate used in this work can be electrically programmed because of the FG structure, which makes the calibration of the sensor possible. Fig. 3.9 (a) and (b) show the double-sweep pulsed IV (PIV) curves of the programmed SWNT sensor and PEI-SWNT sensor, respectively. The V_{th}s of both sensors are shifted to positive direction after programming compared to the results in Fig. 3.7. The inset shows pulse scheme for PIV. Pulsed gate biasing limits the time of charge trapping and detrapping and reduces I-V hysteresis. In Fig. 3.9, the I-V hysteresis of the PEI-SWNT sensor is removed by pulse measurement but the I-V hysteresis of the SWNT sensor still exists. By coating SWNT network with PEI and applying the pulse measurement, the I-V hysteresis in the sensor is nearly eliminated.

Fig. 3.10 (a) and (b) show the dry CO_2 sensing properties of the PEI-SWNT

sensor measured by applying DC biases at 25ºC after one day and 2 weeks, respectively, after PEI coated SWNTs are deposited on the sensor platform. In Fig. 3.10 (a), the drain current decreases when the sensor is exposed to CO_2 target gas sample. However, after two weeks (Fig. 3.10 (b)), the sensor has barely no response to dry CO_2 gases. This may be attributed to the effect of moisture on the CO_2 detection. It seems that the water left in the sensing material is fully evaporated within two weeks and the response to CO_2 is degraded. Therefore, it is necessary to investigate the effect of moisture on CO_2 gas detection using PEI-SWNT sensor.

Fig. 3.11 shows wet CO_2 sensing properties of the PEI-SWNT sensor with the sensing material formed two weeks before the measurement. DC biases are applied to the sensor. Before measuring, we humidify the sensing material by blowing humid air into the sensor for 3 hours. During the wet CO_2 measurement, the relative humidity (RH) of the gas is set to be 30%. With the help of water vapor within the target gas sample, the drain current decreases with the increase of CO_2 concentration again. It indicates that the PEI-SWNT sensor requires moisture for the detection of CO_2 at room temperature. Both CO_2 gas and water vapor involve

in the reaction with the sensing material and decrease the drain current.

As shown in Figs. 3.10 and 3.11, there is drift in the drain current over time. It has a significant impact on the accuracy of CO_2 detection. Hence, a pulse scheme for transient measurement is introduced to obtain reliable measurement results without drift. The pulse scheme is shown in Fig. 3.12 (a). An appropriate pre-bias (V_{pb}) and read bias (V_r) are applied sequentially to the CG. Note that when V_{pb} is applied to the CG, V_{DS} is set to 0 V simultaneously to remove unwanted power consumption. In read biasing period, both V_r and V_{DS} are synchronized and have finite biases. During the read period, the drain current of the sensor will be read out and recorded as the sensing signal. Here, the width of V_{pb} pulse (t_w) and V_r pulse (t_r) are set to 1 s and 50 μs, respectively. Fig. 3.12 (b) shows wet CO_2 (30% RH) detection characteristics of the PEI-SWNT sensor obtained by applying the pulse scheme at room temperature. The drift is removed by the pulse measurement method. In Fig. 3.12, our sensor shows a *response* of 16%, a t_{RES} of 81 s and a t_{REC} of 202 s for 2000 ppm of CO_2 at 25ºC.

In this section, the measurement results show that the PEI-SWNT sensor can

detect CO_2 at room temperature with the help of water vapor. The current drift was removed by using pulse measurement method and the sensor presented short response and recovery speeds, and reasonable response amplitude. However, the PEI-SWNT needs water vapor for CO_2 detection, which may limit the application of the sensor in the real gas detection.

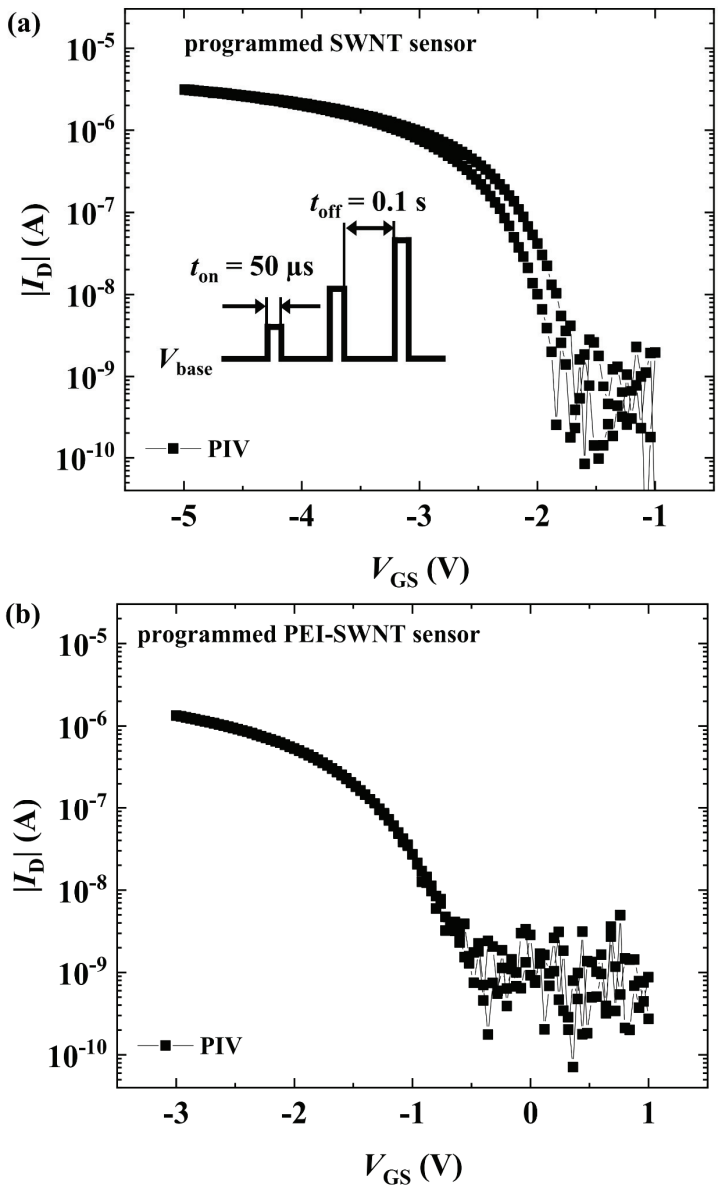

Fig. 3.9 Double-sweep PIV curves of the SWNT sensor (a) and the PEI-SWNT sensor (b) at 25ºC after programming.

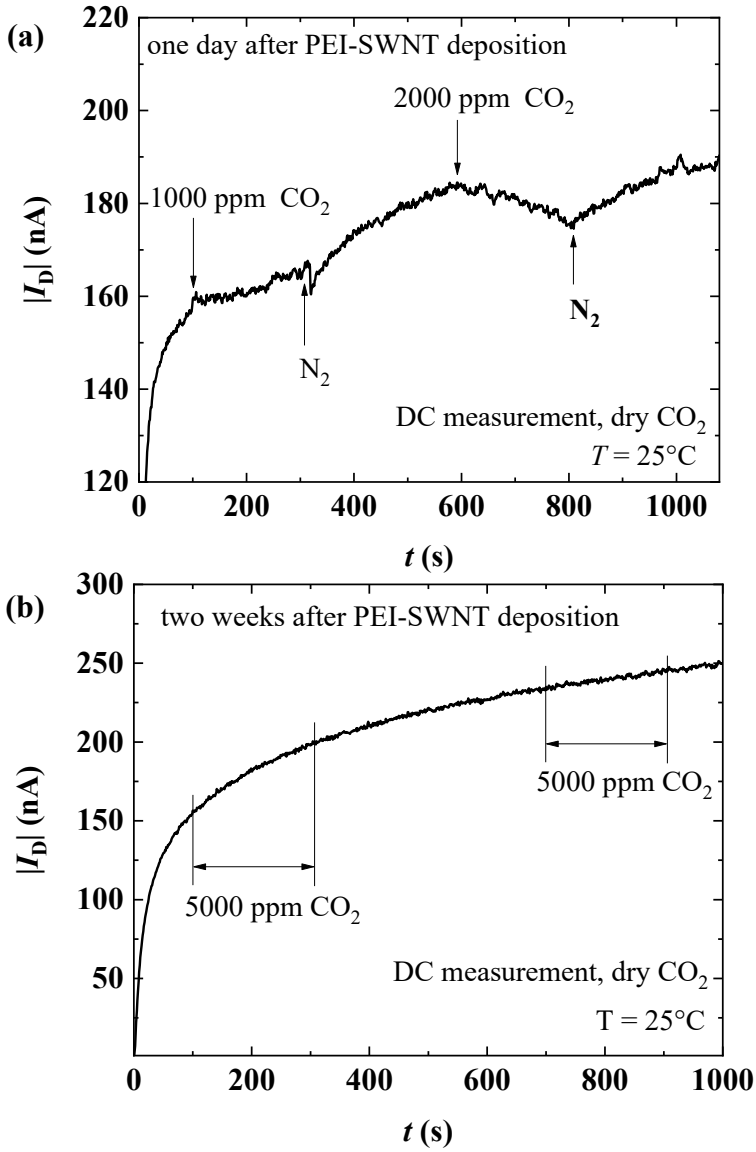

Fig. 3.10 Dry CO_2 sensing properties of the PEI-SWNT sensor measured by applying DC biases at 25ºC after one day (a) or two weeks (b) after the sensing material is deposited.

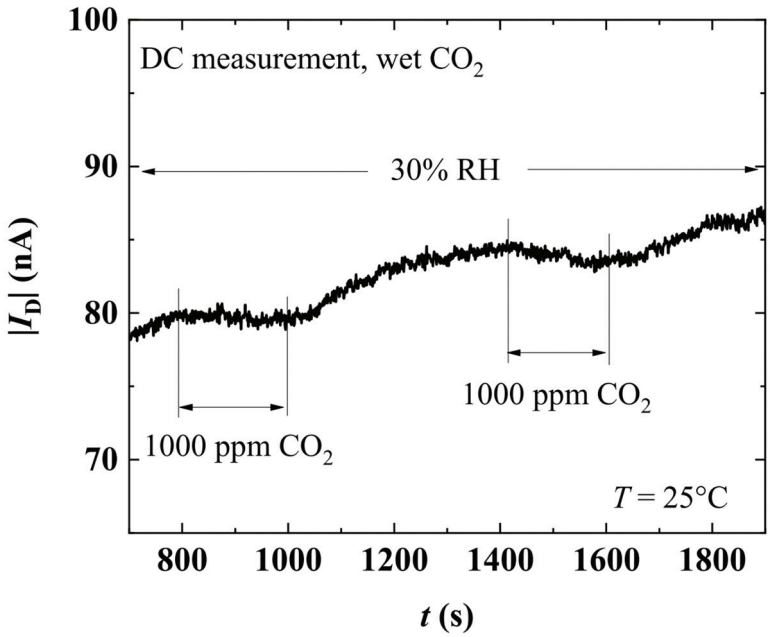

Fig. 3.11 Wet CO_2 detection characteristics of the PEI-SWNT sensor measured by applying DC bias at 25ºC.

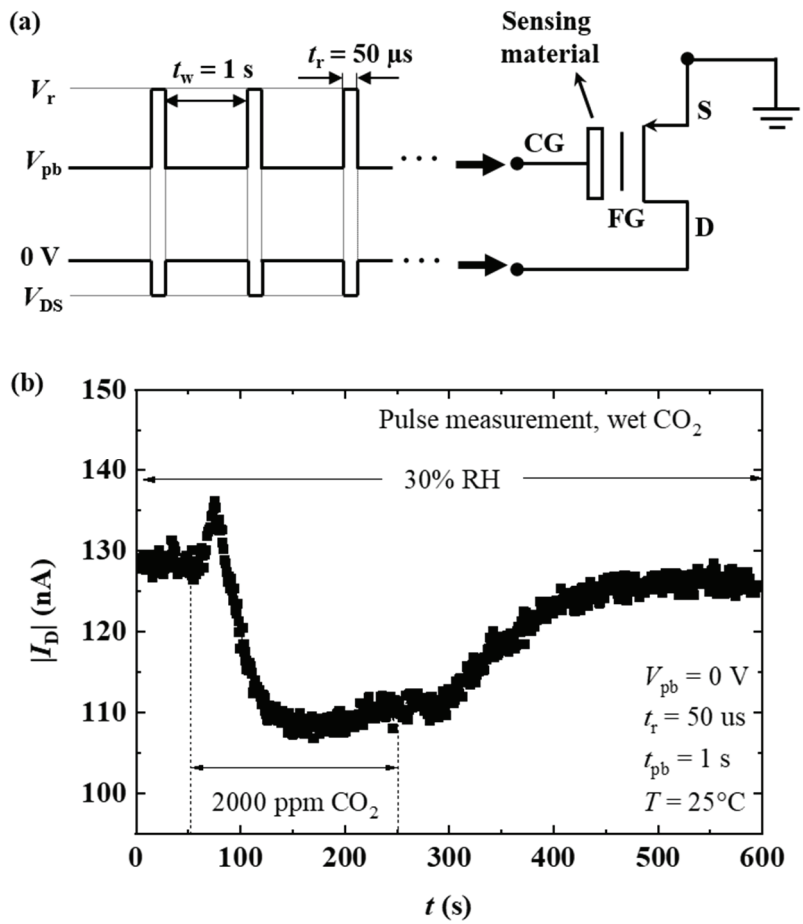

Fig. 3.12 (a) Voltage pulse scheme for measuring sensing characteristics. (b) Wet CO_2 detection characteristics of the PEI-SWNT sensor measured by applying the voltage pulse at 25ºC.

3.3 Na^+ ionic conducting CO_2 sensor

In sections 3.1 and 3.2, CO_2 sensors based on PVA and PEI-SWNT are investigated at room temperature. Both of them need water vapor to react with CO_2 during the detection. In this section a sensing material of Na_2CO_3 and $NaNO_2$ compound is used for CO_2 detection. The working temperature is around 160°C. Between the substrate and the sensing material, an APTES SAM layer is formed. Without this APTES layer, the Na^+ ions will penetrate into the oxide very easily during heating process and induce large leakage current. In section 3.3.1, the function of APTES is addressed. In section 3.3.2, the sensing performance of the Na^+ ionic conducting CO_2 sensor is measured. Finally, the sensor is programmed and the sensing properties of programmed sensor is characterized in section 3.3.3.

3.3.1 APTES SAM ion-blocking layer

As described above, APTES SAM was formed on the oxide surface of the ONO stack in the exposed interdigitated FG-CG region to prevent the penetration of Na^+ ions. A comparison of electrical characteristics between the devices with and without APTES SAM is carried out to demonstrate the ion-blocking capability of the APTES. Fig. 3.13 (a) and (b) plot the I_D-V_{CGS} curves of the sensors with and without the APTES ion-blocking layer, respectively, as a parameter of temperature (20ºC and 160ºC). The insets in both figures show the CG leakage currents (I_G). When the sensing layer directly contacts with the ONO passivation layer covering the FG, the Na^+ ions contained in the sensing material penetrate through the passivation layer during annealing process. It seems that the diffusion of the Na^+ ions makes many leakage paths through the insulator layers. The inset in Fig. 3.13 (a) shows very high CG leakage current (~10 nA) even at 20ºC. Fig. 3.14 illustrates the penetration of Na^+ ions (Fig. 3.14 (a)) and the protective effects of the APTES monolayer (Fig. 3.14 (b)). In Fig. 3.13, the drain current exhibits significant fluctuation and quite poor modulation with the change of the CG bias. The

penetrated ions create paths from the gate to the source resulting in the high gate leakage current. At the same time, the large number positive Na^+ ions inside the oxide near the channel can attract additional electrons making the large off state current and give rise to more scattering. Conversely, the APTES SAM formed on top of the passivation layer effectively blocks the diffusion of the Na^+ ions so that the gate leakage is negligible (less than 10^{-13} A) and reasonable I_D-V_{CGS} curves are obtained as shown in Fig. 3.13 (b).

An APTES molecule consists of a head group, a tail and a functional group (-NH_2 groups) [41]. The "head group" assemble itself on the surface of the ONO stack through the chemical reaction with the -OH groups. The tail and functional group are located far from the stack. As the schematic shows in Fig. 3.15, the -NH_2 groups will capture Na^+ ions and form a complex of APTES-Na^+ [42]–[45]. In this way, the mono APTES layer kept Na^+ ions away from the ONO stack.

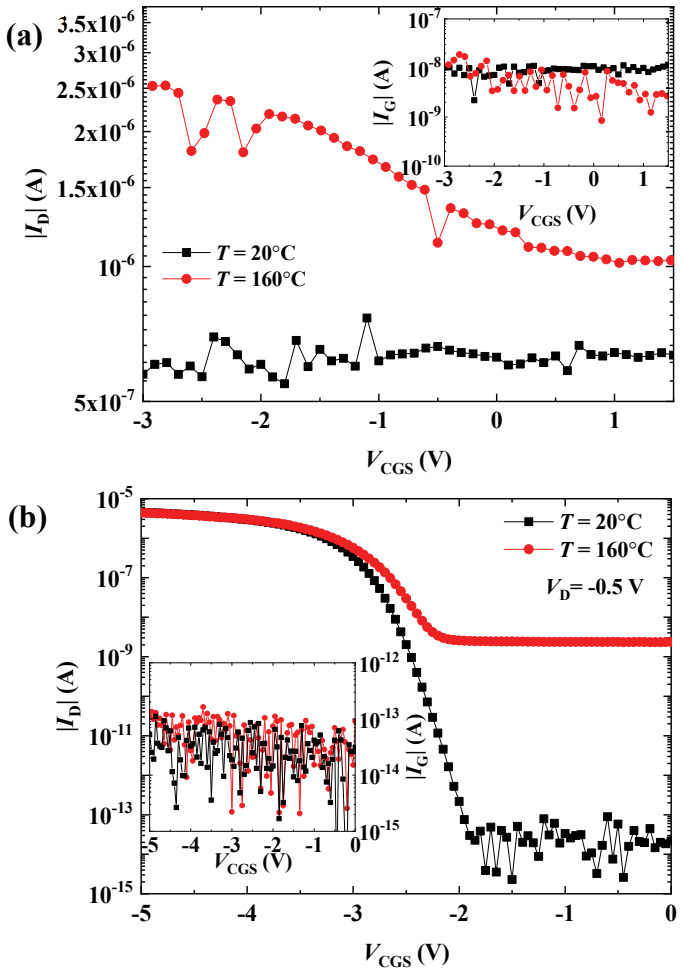

Fig. 3.13 I_D-V_{CGS} characteristics showing Na^+ ion-blocking capability of APTES SAM. Figures (a) and (b) show the I_D-V_{CGS} curves of the sensors with and without the APTES ion-blocking layer, respectively, as a parameter of measurement temperature (20ºC and 160ºC). The insets plot the I_G-V_{CGS} curves showing the control-gate leakage current.

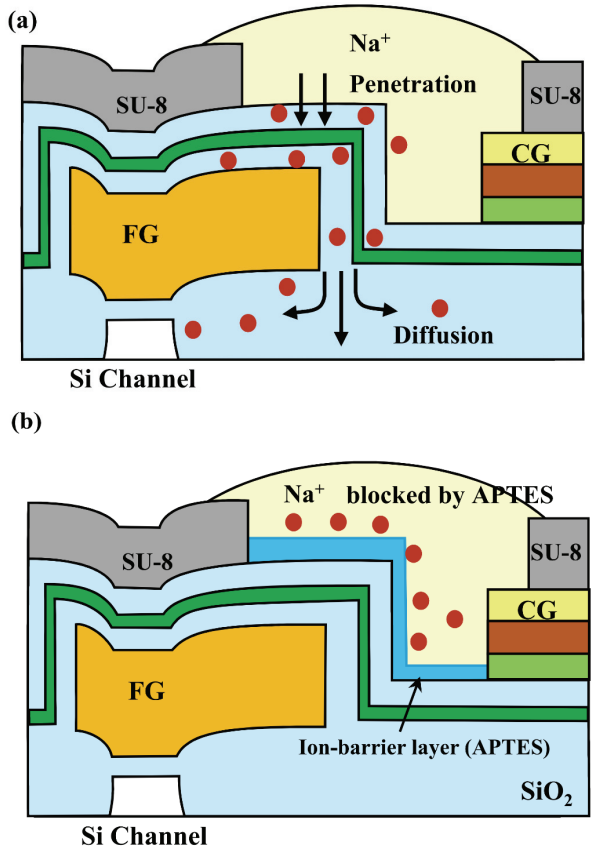

Fig. 3.14 (a) The penetration of Na ions. (b) The protective effects of the APTES monolayer.

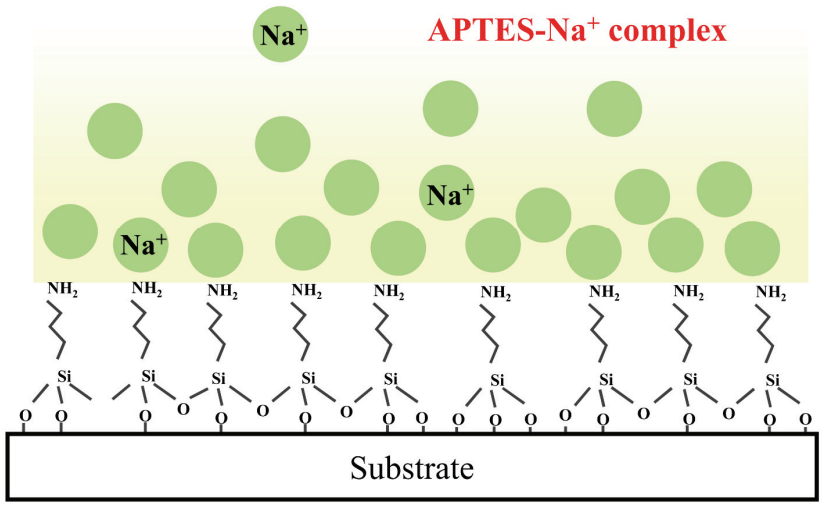

Fig. 3.15 The –NH_2 functional groups capture Na^+ ions and form a complex of APTES-Na^+ to prevent the penetration of Na^+ ions.

Fig. 3.16 (a) and (b) shows the I_D-V_{CGS} curves of three FET sensors having three different materials on the exposed interdigitated FG and CG: nothing (air) (Fig. 3.16 (c)), APTES only (Fig. 3.16 (d)), and both APTES and sensing materials (Fig. 3.16 (e)) at different temperatures. Note the three sensors have the same geometries and structure, and were fabricated on the same silicon substrate. The device having both APTES and sensing material is working properly as a normal

*p*MOSFET with negligible gate leakage current at both 20ºC and 160ºC. However, the FET sensor with air or APTES only cannot be turned on even at a CG bias of −6 V no matter at 20ºC or 160ºC, because the capacitive coupling between the CG and the FG is too low compared to that between the FG and the channel. The results in Fig. 3.13 and Fig. 3.16 conclude that the sensing layer enhances the capacitive coupling ratio between CG and FG. In addition, the APTES ion-blocking layer effectively prevents the Na^+ ion leakage and will not affect the electrical characteristics of the *p*MOSFET because its thickness is only about 1 nm [46]–[49]. It makes the Na^+-ion-conducting solid electrolyte compatible with the FET-type sensor platform.

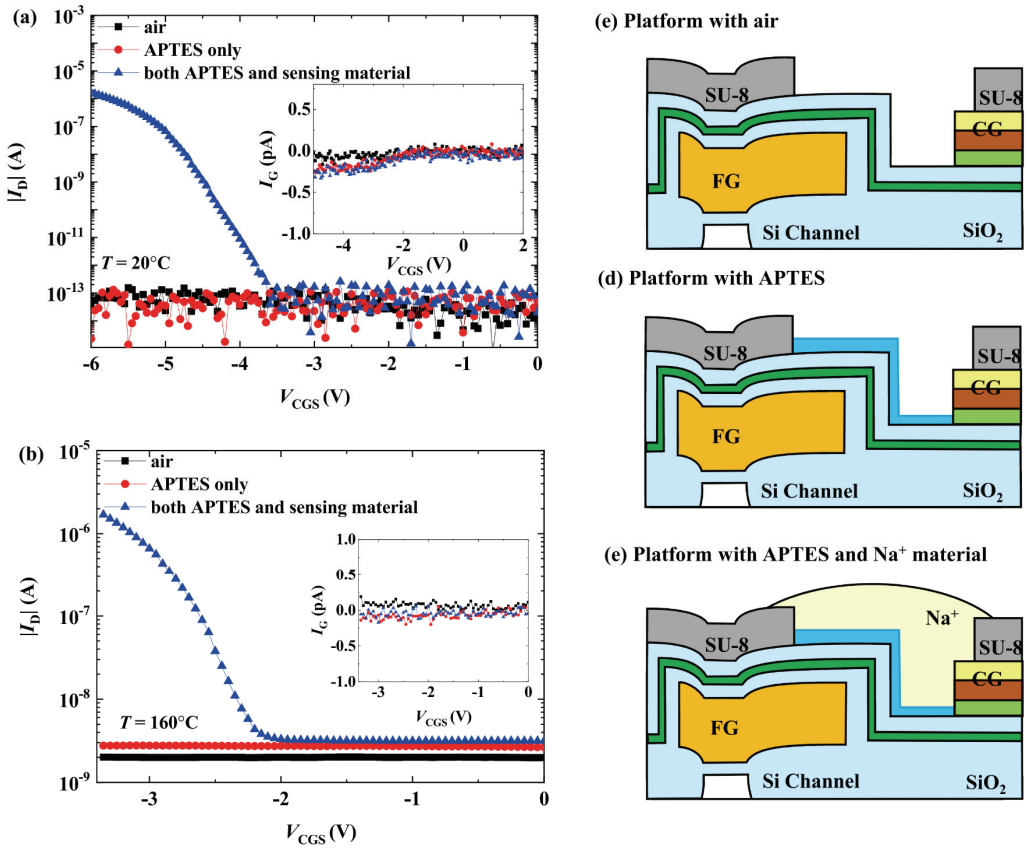

Fig. 3.16. I_D-V_{CGS} curves of three FET platforms having different materials (nothing (air), APTES SAM only, both APTES SAM and sensing material) on the exposed interdigitated FG and CG at measurement temperatures of 20ºC (a) and 160ºC (b). The insets are the I_G-V_{CGS} curves.

Except APTES, two more SAM materials, n-octadecyltrichlorosilane (ODTS) and 1H,1H,2H,2H-Perfluorooctyltriethoxysilane (F-OTS) are also investigated for comparison. After forming the two SAM layers separately on two FET sensor substrates, the Na^+-ion-conducting material (Na_2CO_3 and $NaNO_2$ with a molar ratio of 1:3) are printed on both two substrates using the same process described in Chapter 2. The formulas of ODTS and F-OTS are shown in Fig. 3.17. The functional groups of APTES, ODTS and F-OTS are $–NH_2$, $–CH_3$, and $–CF_3$, respectively. Fig. 3.18 plots the I_D-V_G and I_G-V_G curves of sensors with ODTS and F-OTS at 20ºC. Large leakage currents are found in both ODTS and F-OTS sensors. Even though ODTS and F-OTS can also assemble on the surface of the substrates to form monolayers between the sensing material and the FET substrates, the Na+ ions still can easily penetrate into the oxide resulting in large leakage current. It indicates that the specie of functional groups determines the ion preventive capability of the SAM layer. In a word, Only the APTES of the investigated three SAM materials reacts with Na^+ ions producing APTES-Na^+ complexes and presents an outstanding ion blocking effect.

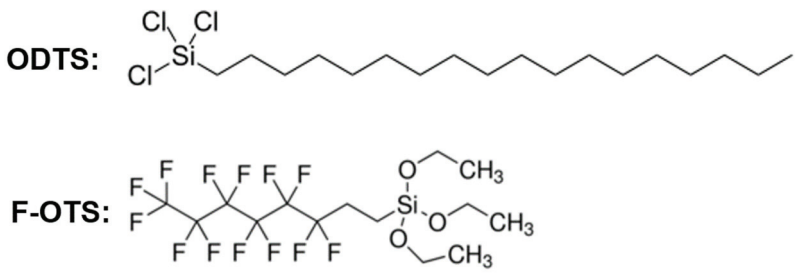

Fig. 3.17 The chemical formulas of ODTS and F-OTS. The functional groups of ODTS and F-OTS are $–CH_3$, and $–CF_3$, respectively.

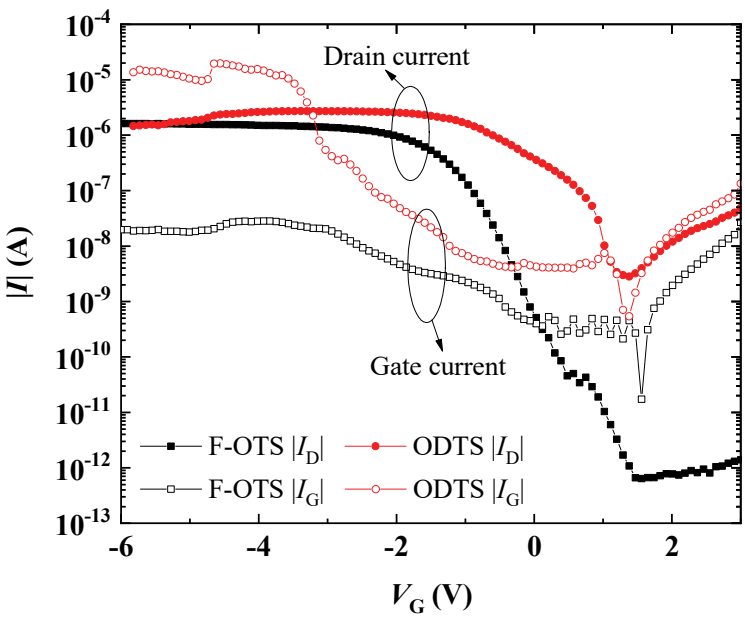

Fig. 3.18 I-V curves of sensors with ODTS and F-OTS at 20ºC. Large leakage currents are found in both ODTS and F-OTS sensors.

3.3.2 Gas sensing performance

Fig. 3.19 (a) shows the CO_2 sensing performance of the proposed sensor with N_2 as the reference gas and (b) shows the track of gate leakage current. The operating temperature here is 160ºC for good stability of the sensor, relative low heat power consumption and relative high ionic conductivity [50]. Constant biases are applied to the CG and drain electrodes to keep a certain absolute drain current level ($|I_D|$). The $|I_D|$ is changed and recorded as the sensing signal by changing the ambient gas. First, the sensor is held in a test chamber filled with N_2. When the $|I_D|$ of the sensor saturates after a-few-minute drift, a target gas consisting of 180 ppm of CO_2 and dry synthetic air is provided to the chamber. The $|I_D|$ is increased by the target gas.

According to Fig. 3.19, *response*=133%, t_{RES}=550 s and t_{REC}=820 s for 180 ppm of CO_2 at 160ºC. A fluctuation in the $|I_D|$ is observed when the sensor is starting to approach saturation. It may result from the physical and chemical processes taking place at the gas/gate metal/Na^+-ion-conducting material three-phase-boundary (TPB) [51].

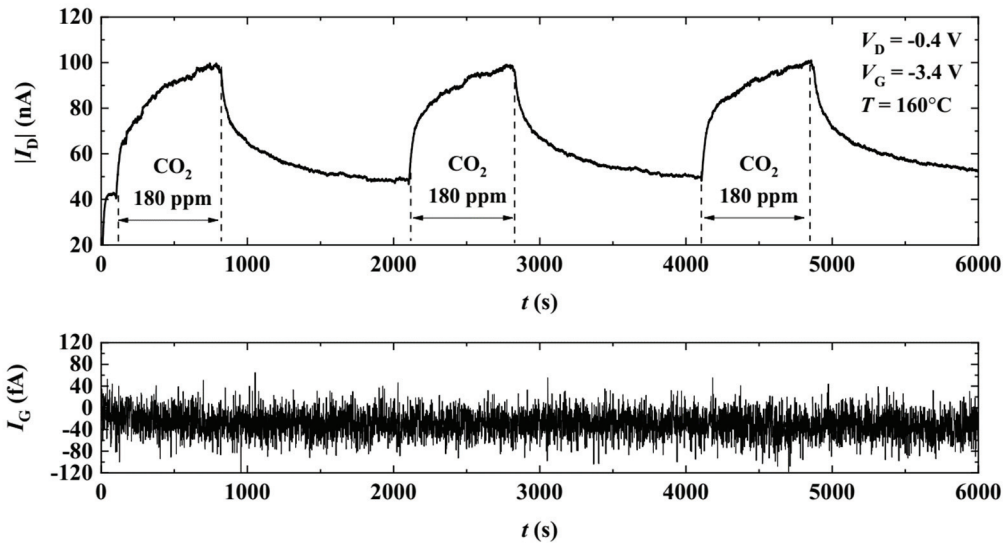

Fig. 3.19 CO_2 sensing performance of the proposed sensor with N_2 as the reference gas at 160ºC. The increase of CO_2 concentration induces the increase of the drain current $|I_D|$.

3.3.3 Programming of the FET sensor platform

Due to the FG of our FET-type sensor platform, the sensor can be programmed or erased just like a common memory device. The V_{th} of the sensor can be controlled by the programming and erasing conditions (programming/erasing voltages and time), which is beneficial to the calibration and the adaptation of the sensor to meet different operating requirements [52]. In Fig. 3.20, the sensor is programed by the condition of V_G=15 V at V_D=V_S=0 V for 10 s at 150ºC and the V_{th} is shift to the positive direction by about 5 V. In this way, a reasonable current can be obtained by applying a very small CG bias or even zero CG bias.

The I_D-V_{CGS} curves of the sensor before and after programing are plotted in Fig. 3.20 (a). The $|I_D|$ transient curve of the sensor in N_2 ambient after programing is shown in Fig. 3.20 (b), which indicates stability of the sensor. Fig. 3.21 (a) shows the sensing performance of the programed sensor for 500 ppm CO_2 with N_2 reference gas at 150ºC. Note that V_{CGS}=0 V during the measurement, and the MOSFET works in the linear region according to the I_D-V_{CGS} curve in Fig. 3.20. Fig. 3.21 (b) shows ΔI_D (ΔI_D=$|I_{D\_G}|$−$|I_{D\_B}|$) as the function of CO_2 concentration at

150ºC after programming. Here, the reference gas is synthetic air in place of N_2. To remove the influence of O_2 on the sensing performance, we keep a constant proportion of the O_2 in both the reference gas and the target gas sample by balancing the concentration of CO_2 with N_2. The ΔI_D increases with the increase of CO_2 concentration.

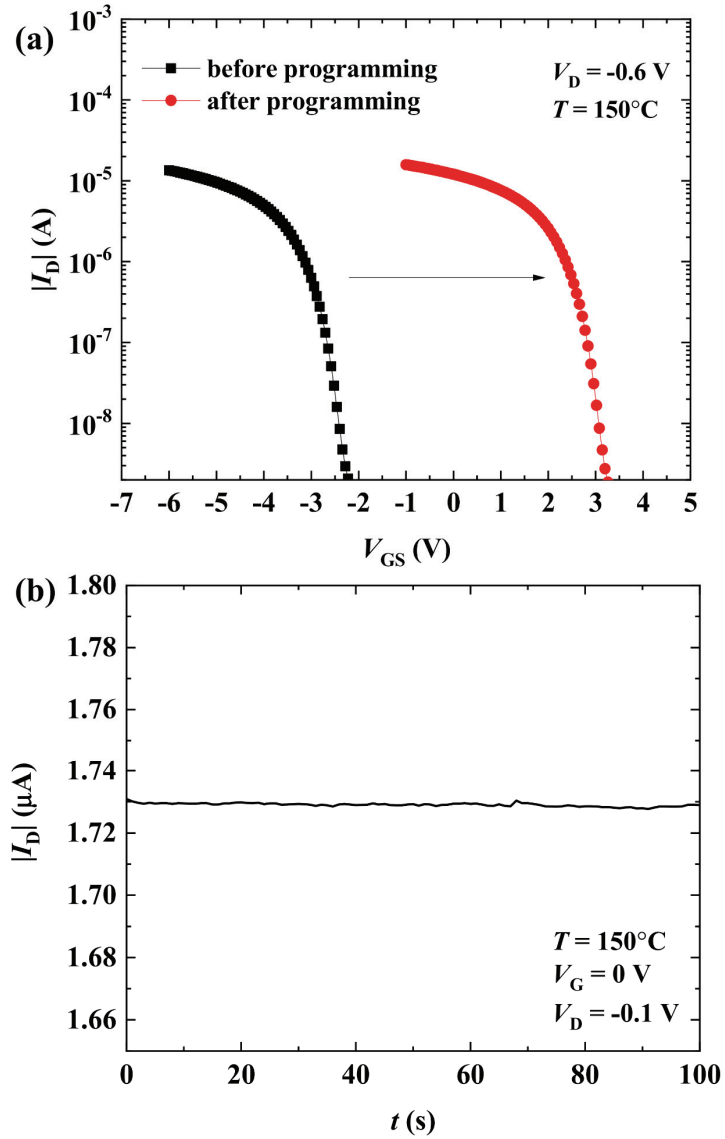

Fig. 3.20 (a) The *I-V* curves of the sensor before and after programing. (b) I_D transient curve of the sensor in N_2 ambience after programing.

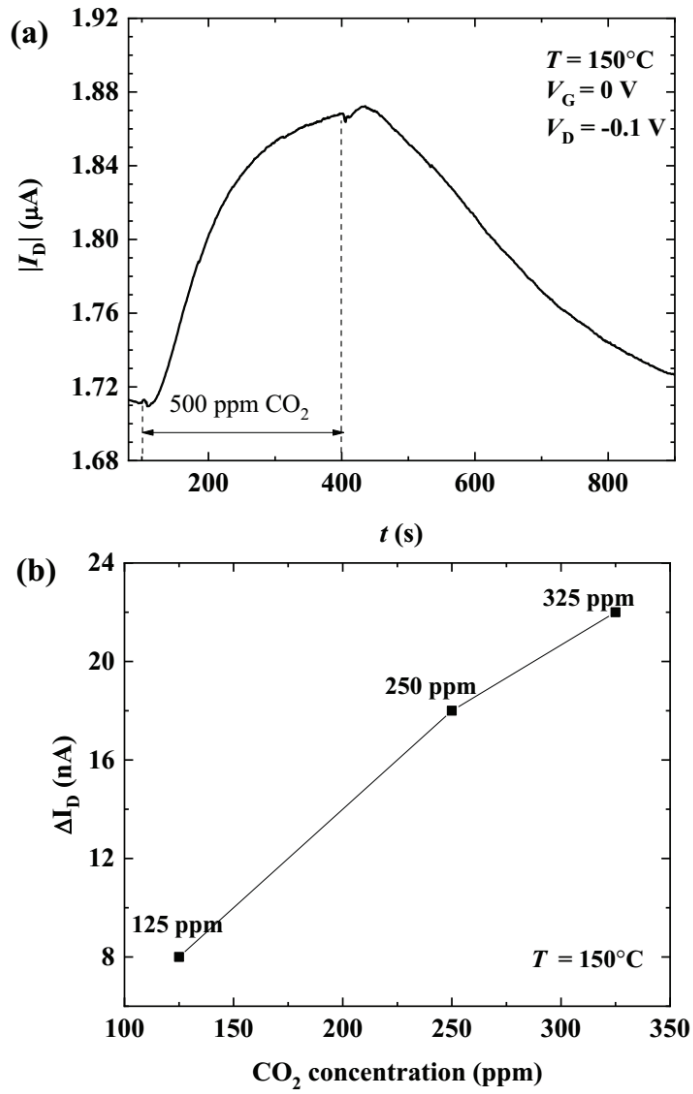

Fig. 3.21 (a) Sensing performance of the programed sensor for 500 ppm CO_2 with N_2 reference gas at 150ºC. (b) ΔI_D as the function of CO_2 concentration after programming the sensor. $\Delta I_D = |I_{D\_G}| - |I_{D\_B}|$.

Chapter 4

Device sensing mechanism

4.1 Sensing mechanism of PEI-SWNT sensor

By comparison, the sensors with Na^+ ionic conducting material and PEI-SWNT present more reasonable sensing performance than the sensor with PVA in Chapter 3. Therefore, in this chapter, the sensing mechanism of the sensors with Na^+ ionic conducting material and PEI-SWNT will be discussed. This section explains the CO_2 sensing mechanism of the sensor with PEI-SWNT.

SWNT is a kind of p-type semiconductor which has been developed for the detections of various gases, such as NO_2, NH_3, H_2S, CO, SO_2 and volatile organic compounds. In this work, the polymer PEI is deposited to cover the random SWNT network to reduce the I-V hysteresis as discussed in Chapter 3. Without dopants, it is a kind of dielectric substance. The PEI molecules dispersed the nanotubes and reduced the number of the interface traps between SWNTs and oxide, and the traps inside the sensing layer. As reported in literature [53], the PEI coating can also

generate a n-type doping to the SWNTs, and result in a transition of SWNT from p-type to n-type semiconductor.

Some reports suggested that the PEI coated carbon-based materials can detect CO_2 because of the electron transportation [54]. The PEI wraps the nanotubes and changes SWNT from p-type to n-type by supplying more electrons. During the CO_2 detection, the CO_2 molecules react with PEI and affect the electron transportation in SWNTs. As a result, the resistance of SWNTs will be changed. Nevertheless, some research groups found that the CO_2 adsorption can lead to a capacitance change inside the amino functional sensing materials [55]. In reference [56], the authors proposed a capacitive CO_2 sensor by using a mixture of MWNT and SiO_2 as the sensing material. The increase of CO_2 concentration resulted in a permittivity decrease of the sensing material. Moreover, in literature [56], a mixture of 3-Aminopropyltrimethoxysilane (AMO) and Propyltrimethoxysilane (PTMS) (7:3 in volume) was used to detect CO_2 at 22ºC with measuring the capacitance of the sensing material. The sensing material is filled with amino groups that can react with CO_2. The measurement results showed a decrease of capacitance when the

concentration of CO_2 increased.

The branched PEI used in this work has a large amount of amino end groups inside, which are primary, secondary, and tertiary amines in a ratio of 1:1.2:0.76. All these amines can be involved in the reactions with CO_2 especially in the presence of water vapor, and form ammonium carbamate and/or ammonium bicarbonate species. The related reactions are presented as Fig. 4.1 [57]. Therefore, we suggest a hypothesis about the sensing mechanism that the change in the sensor is caused by the PEI reaction with CO_2 molecules and it is the capacitance change of the sensing material that induces the drain current change.

Fig. 4.2 shows the equivalent circuit of the sensor in (b) along A-A' in (a). The PEI-SWNT sensing material is reproduced by a series connection of a resistor R_{CG} and a capacitor C_{CG}. The C_{pass}, C_{FG} and C_p are the ONO, floating gate, and parasitic capacitances, respectively. We define γ the gate coupling coefficient between the CG and the FG. Then γ can be expressed as

$$\gamma = (C_{CG} \parallel C_{pass})/\left[\left(C_{CG} \parallel C_{pass}\right) + C_p + C_{FG}\right] \quad (2)$$

During CO_2 detection, the reaction between CO_2 and the sensing material

changes the capacitance of the sensing material C_{CG}. This change will be transferred to the FG of the FET substrate through the gate coupling coefficient γ according to equation (2). As the FET substrate has a FG, the threshold voltage V_{th} relative to FG can be written as [58]

$$V_{th} = \phi_{ms} - \frac{Q_{ox}}{C_{ox}} + 2\psi_B - \frac{\sqrt{2qN_D\varepsilon_{Si}|2\psi_B|}}{C_{ox}} \quad (3)$$

As the *p*-MOSFET platform is used in this work, the ψ_B in equation (3) is negative, which is defined as the difference between the Fermi level and the intrinsic energy level of the silicon substrate. The ϕ_{ms} is the work-function difference between gate and Si substrate, the Q_{ox} is the equivalent oxide charge per unit area at the oxide-silicon interface, and the N_D is the doping concentration of the body. The C_{ox} equals to the C_{FG}. Consequently, the drain current of the FET substrate in the subthreshold region and linear region can be written as equation (4) and (5), respectively.

$$|I_D| = \mu C_{FG} \frac{W}{L} \sqrt{\frac{\epsilon_{si} q N_d}{4\psi_B}} \left(\frac{kT}{q}\right) e^{q(|\gamma V_{CGS} - V_{th}|)/mkT} \quad (4)$$

$$|I_D| = \mu C_{FG} \frac{W}{L} [|\gamma V_{CGS} - V_{th}| + mV_{DS}/2] V_{DS} \quad (5)$$

When the concentration of CO_2 increases, the C_{CG} decreases, which

deteriorates the gate coupling coefficient γ according to equation (2). As a result, the drain current $|I_D|$ decreases according to equation (4) and (5). During the recovery of the sensor, the adsorbed CO_2 molecules will be released from the sensing material. Then the C_{CG} increases and induces the increase of coefficient γ. As a result, the drain current $|I_D|$ increases.

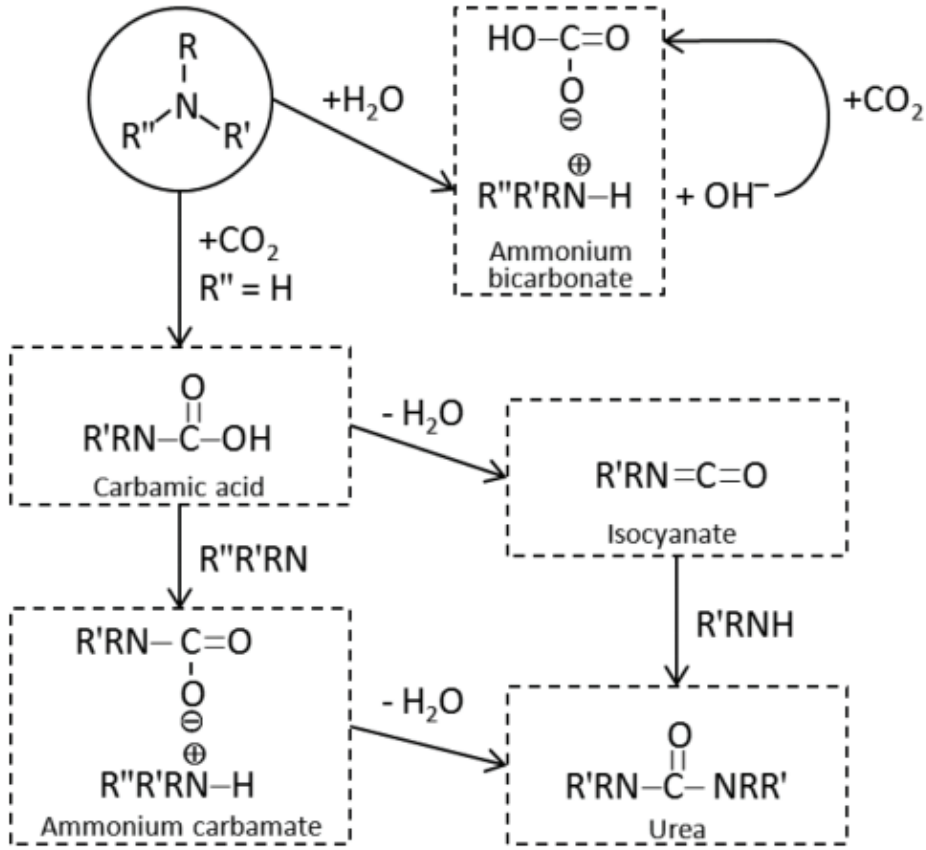

Fig. 4.1 Related reactions and chemical species involved in the adsorption of CO_2 by PEI. The R, R', and R'' are either organic substituent of hydrogen atoms [57].

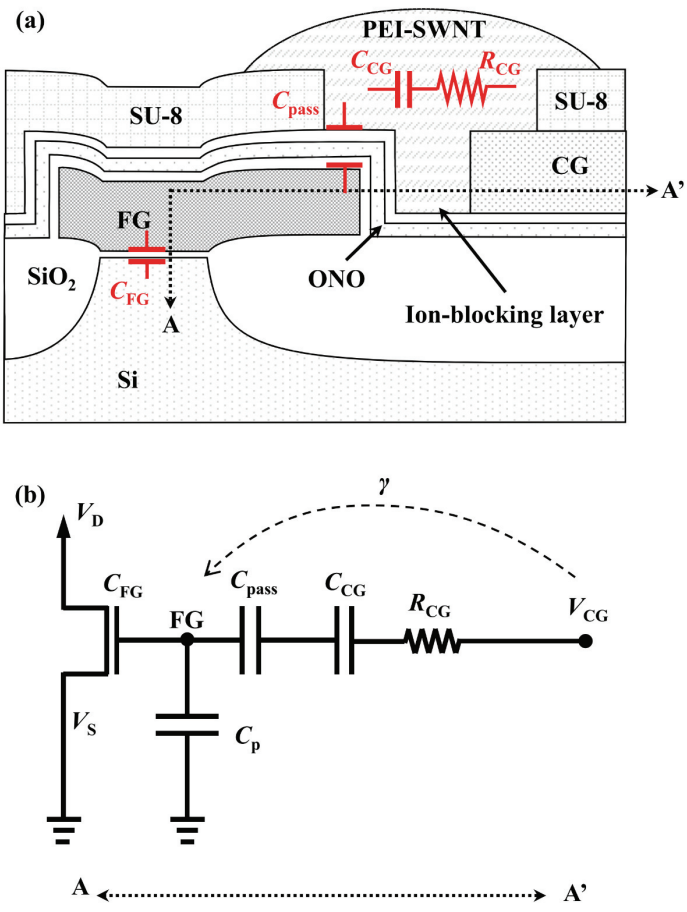

Fig. 4.2 The equivalent circuit of the sensor with PEI-SWNT. (a) The sensing material is simplified as a series connection of the R_{CG} and C_{CG}. The C_{pass}, C_{FG} and C_p are the ONO passivation, floating gate, and parasitic capacitances, respectively. (b) shows the equivalent circuit of the sensor along A-A' in (a). The γ refers to the gate coupling coefficient between the FG and CG.

4.2 Sensing mechanism of the sensor based on Na^+ conducting material

As discussed in Chapter 2 and Chapter 3, the compound of Na_2CO_3 and $NaNO_2$ (the molar ratio is 1:3) is deposited on the surface of the FET sensor substrate to serve as the sensing material for the detection of CO_2 gas. According to the measurement results in Chapter 3, without APTES ionic blocking layer, Na^+ ions can freely reach to the oxide and cause serious operating problems such as large gate leakage current and off-state current, and significant fluctuation in drain current. In contrast, with the help of APTES, the sensor can be operated as a common MOSFET and detect CO_2 gas at an appropriate working temperature. This indicates that, with the deposition process described in Chapter 2, there is a large number of mobile Na^+ ions existing inside the sensing material. These Na^+ ions move easily inside the sensing material and correspond to the negative fixed ions. When operating the sensor, the source is grounded and certain voltages are applied to the gate and the drain electrodes to obtain a reasonable drain current. Fig. 4.3 shows the schematic of the charge distribution within the sensor during the

operation. The positive Na^+ ions and the negative ions will distribute according to the electric field across the sensing material and affect the number of carriers in the channel of the FET [59], [60].

Fig. 4.4 shows the equivalent circuit of the sensor with Na^+ ionic conducting material. In Fig. 4.4 (a), the sensing material is simplified as a capacitance denoted as C_{sens} [61] (including all the capacitance at the interfaces and in the bulk of the sensing material). The C_{pass}, C_{FG} and C_p are the APTES-covered ONO, floating gate, and parasitic capacitances, respectively. Note that the C_{pass} also involves the capacitance of the APTES monolayer. Fig. 4.4 (b) shows the equivalent circuit of the sensor from A to A' in (a). Appropriate V_{CG} and V_D are applied to the CG and drain electrodes, and V_S = 0 V to obtain a reasonable drain current during the operation. The point B in (a) is at the interface between the sensing material and the APTES, which is corresponding to the point B in the equivalent circuit in (b). The potential drop V_{sens} resulting from C_{sens}, which is the potential difference across the sensing material (from CG to point B), is determined by the concentration of CO_2. Then, the potential at the point B in Fig. 4.4 (b), V_{CG}', can be written as

$$V'_{CG} = V_{CG} - V_{sens} \tag{6}$$

For the sensor with Na^+ ionic conducting material, we define γ as the gate coupling coefficient relative to the point B rather than the CG metal in Fig. 4.2. In another word, the C_{sens} is not involved in the γ. Then the γ of the sensor with Na^+ ionic conducting material can be represented as

$$\gamma = C_{pass}/\left(C_{pass} + C_p + C_{FG}\right) \tag{7}$$

Then the voltage of the FG is

$$V_{FG} = \gamma V_{CG}{}' = \gamma(V_{CG} - V_{sens}) \tag{8}$$

Therefore, when $|V_{DS}| > 2kT/q$, the drain current in subthreshold region is

$$|I_D| = \mu C_{FG} \frac{W}{L} \sqrt{\frac{\epsilon_{si} q N_d}{4\psi_B}} \left(\frac{kT}{q}\right) e^{q(|\gamma(V_{CGS} - V_{sens}) - V_{th}|)/mkT} \tag{9}$$

The drain current in linear region is

$$|I_D| = \mu C_{FG} \frac{W}{L} [|\gamma(V_{CGS} - V_{sens}) - V_{th}| + mV_{DS}/2]V_{DS} \tag{10}$$

The V_{th} here is the same as defined in equation (3), which refers to the threshold voltage with respect to the FG.

During the gas response period, the CO_2 molecules will diffuse into the sensing material and react with Na^+ ions. Some reports [50] suggest the involved

electrochemical reaction as

$$2Na^+ + CO_2 + \frac{1}{2}O_2 + 2e^- \rightleftharpoons Na_2CO_3 \quad (11)$$

The mobile Na^+ ions will be consumed by this reaction with producing neutral Na_2CO_3 molecules. In this way, the total number of Na^+ ions are reduced, so that the distribution of Na^+ ions inside the sensing material (C_{sens}) is changed. Then the potential difference V_{sens} across the sensing material is reduced, which results in the increase of the $|I_D|$ according to equations (9) and (10).

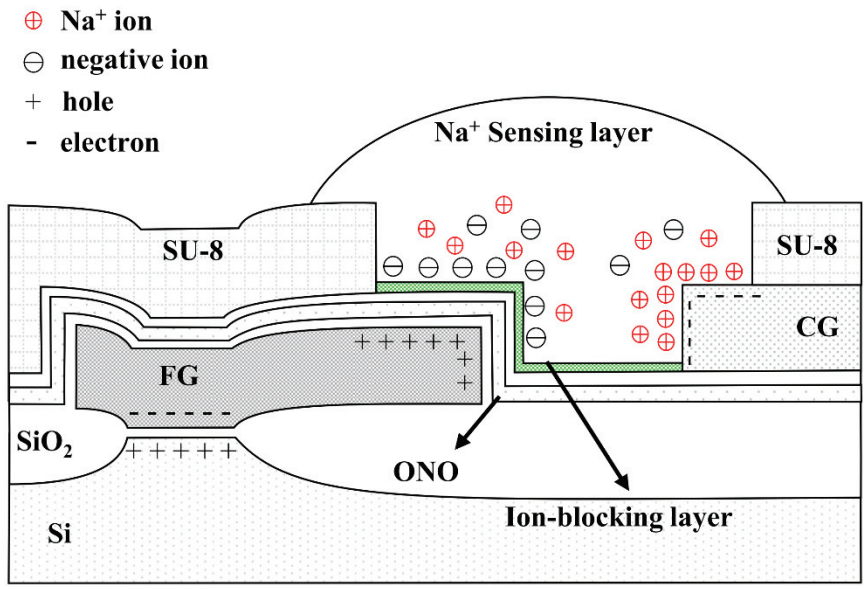

Fig. 4.3 Schematic of the charge distribution within the sensor during the operation.

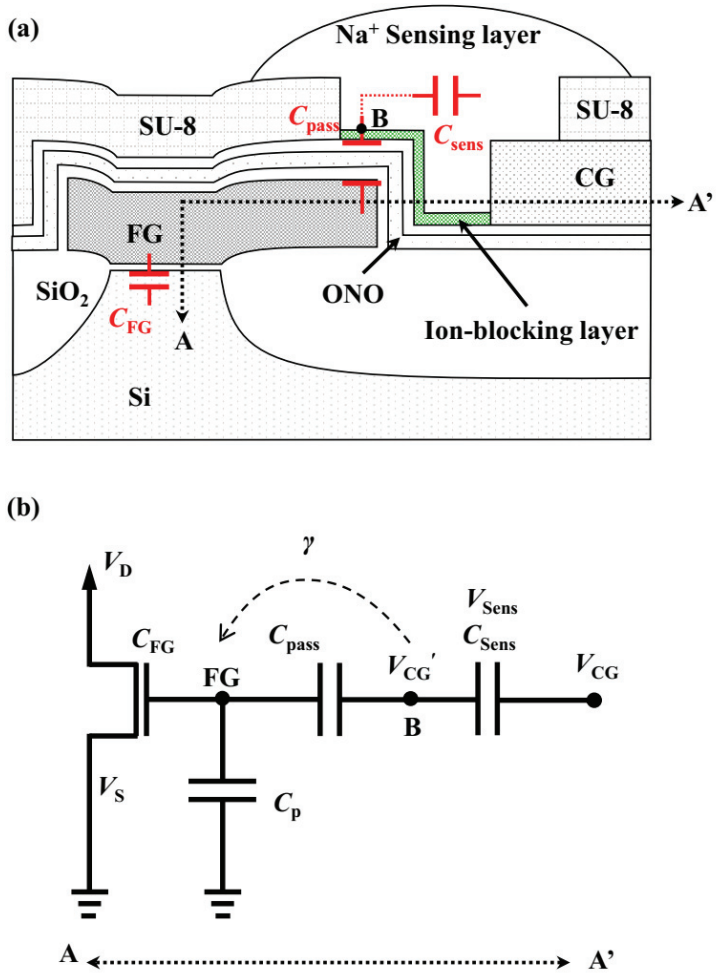

Fig. 4.4 The equivalent circuit of the sensor with Na^+ ionic conducting material. (a) The sensing material is simplified as a capacitor, C_{sens}. The C_{pass}, C_{FG} and C_p are the APTES-covered ONO, floating gate, and parasitic capacitances, respectively. (b) The equivalent circuit of the sensor from A to A' in (a).

Chapter 5

Conclusion

In this dissertation, we investigated CO_2 sensors based on FET platforms working at low temperature. Three different sensing material are developed, which are PVA polymer, PEI-SWNT random network, and Na^+ ionic conducting material. All the materials were deposited on the surface of the FET platform by using inkjet printing process. The basic electrical and gas sensing properties of the sensors were measured. For PVA and PEI-SWNT CO_2 sensor, the working temperature is 25ºC. It was found that the water vapor plays a vital role in their CO_2 detection. The sensor with PVA has short lifetime as it was degraded after 2 weeks after the deposition. By comparison, the sensor with Na^+ ionic conducting material has the most reliable CO_2 sensing behavior. Even though the working temperature of the sensor with Na^+ ionic conducting material is 160ºC, it is still much lower than typical CO_2 sensors. In conclusion, with the help of APTES ion-blocking layer, it turns to be possible to apply the sodium ionic containing material to FET platform, and the sensor with

Na^+ ionic conducting material can be expected to promote the research on low-temperature CO_2 sensor based on Si CMOS technology.

Bibliography

[1] S. Muttamara and S. T. Leong, “Environmental Monitoring and Impact Assessment of a Solid Waste Disposal Site,” *Environ. Monit. Assess.*, vol. 48, no. 1, pp. 1–24, Oct. 1997.

[2] B. D. Jerold, M. P. Kumar, B. Dilip Jerold, and M. Pradeep Kumar, “Experimental investigation of turning AISI 1045 steel using cryogenic carbon dioxide as the cutting fluid,” *J. Manuf. Process.*, 2011.

[3] T. P. Keeling, C.D., Whorf, “Trends A Compendium of Data on Global Change,” *Oak Ridge Natl. Lab.*, 1998.

[4] IPCC, “Climate Change 2014 Synthesis Report Summary Chapter for Policymakers,” *Ipcc*, 2014.

[5] U. S. D. Scripps Institution of Oceanography, “A daily record of atmospheric carbon dioxide,” *the Keeling Curve*, 2018. [Online]. Available: https://scripps.ucsd.edu.

[6] A. J. In, “CO_2 measurement inside meeting, classrooms, offices rooms etc.,” 2018. [Online]. Available: http://www.gasalarm.com.au/importance-of-co2-measurement-inside-meeting-rooms-classrooms-offices-etc/.

[7] T. G. Nenov and S. P. Yordanov, *Ceramic Sensors: technology and application*. Lancaster, PA, USA: Technomic Publishing Company, Inc., 1996.

[8] L. B. Mendes, N. W. M. Ogink, N. Edouard, H. J. C. van Dooren, I. de F. F. Tinôco, and J. Mosquera, “NDIR gas sensor for spatial monitoring of carbon dioxide concentrations in naturally ventilated livestock buildings,” *Sensors*

(Switzerland), 2015.

[9] D. Gibson and C. MacGregor, "A novel solid state non-dispersive infrared CO_2 gas sensor compatible with wireless and portable deployment," *Sensors (Switzerland)*, 2013.

[10] N. Barsan, D. Koziej, and U. Weimar, "Metal oxide-based gas sensor research: How to?," *Sensors Actuators, B Chem.*, 2007.

[11] T. Seiyama and S. Kagawa, "Study on a Detector for Gaseous Components Using Semiconductive Thin Films.," *Anal. Chem.*, 1966.

[12] L. A. Patil, M. D. Shinde, A. R. Bari, and V. V. Deo, "Highly sensitive and quickly responding ultrasonically sprayed nanostructured SnO_2 thin films for hydrogen gas sensing," *Sensors Actuators, B Chem.*, 2009.

[13] S. E. Jo, B. G. Kang, S. Heo, S. Song, and Y. J. Kim, "Gas sensing properties of WO_3 doped rutile TiO_2 thick film at high operating temperature," *Curr. Appl. Phys.*, 2009.

[14] A. Haeusler and J. U. Meyer, "A novel thick film conductive type CO_2 sensor," *Sensors Actuators, B Chem.*, 1996.

[15] S. Matsubara, S. Kaneko, S. Morimoto, S. Shimizu, T. Ishihara, and Y. Takita, "Practical capacitive type CO_2 sensor using CeO_2/$BaCO_3$/CuO ceramics," *Sensors Actuators, B Chem.*, 2000.

[16] D. H. Kim, J. Y. Yoon, H. C. Park, and K. H. Kim, "CO_2-sensing characteristics of SnO_2 thick film by coating lanthanum oxide," *Sensors Actuators, B Chem.*, 2000.

[17] P. Keller, H. Ferkel, K. Zweiacker, J. Naser, J. U. Meyer, and W. Riehemann, "Application of nanocrystalline $BaTiO_3$-composite films as CO_2-sensing layers," *Sensors Actuators, B Chem.*, 1999.

[18] T. Kida, H. Kawate, K. Shimanoe, N. Miura, and N. Yamazoe, “Interfacial structure of NASICON-based sensor attached with Li_2CO_3-$CaCO_3$ auxiliary phase for detection of CO_2,” *Solid State Ionics*, 2000.

[19] J. S. Lee, J. H. Lee, and S. H. Hong, “Solid-state amperometric CO_2 sensor using a sodium ion conductor,” *J. Eur. Ceram. Soc.*, 2004.

[20] I. Lundstrom, M. Armgarth, and L. G. Petersson, “Physics with catalytic metal gate chemical sensors,” *Crit. Rev. Solid State Mater. Sci.*, 1989.

[21] Q. He *et al.*, “Fabrication of flexible MoS_2 thin-film transistor arrays for practical gas-sensing applications,” *Small*, 2012.

[22] M. Fleischer, “Advances in application potential of adsorptive-type solid state gas sensors: High-temperature semiconducting oxides and ambient temperature GasFET devices,” *Measurement Science and Technology*. 2008.

[23] K. Arshak, E. Moore, G. M. Lyons, J. Harris, and S. Clifford, “A review of gas sensors employed in electronic nose applications,” *Sensor Review*. 2004.

[24] K. I. Lundström, M. S. Shivaraman, and C. M. Svensson, “A hydrogen-sensitive Pd-gate MOS transistor,” *J. Appl. Phys.*, 1975.

[25] A. Oprea, N. Bârsan, and U. Weimar, “Work function changes in gas sensitive materials: Fundamentals and applications,” *Sensors Actuators, B Chem.*, 2009.

[26] J. Janata, “Apparatus and method for measuring the concentration of components in fluids,” US4411741A, 1983.

[27] S. Stegmeier, M. Fleischer, and P. Hauptmann, “Thermally activated platinum as VOC sensing material for work function type gas sensors,” *Sensors Actuators, B Chem.*, 2010.

[28] C. H. Kim, I. T. Cho, J. M. Shin, K. B. Choi, J. K. Lee, and J. H. Lee, “A new gas sensor based on MOSFET having a horizontal floating-gate,” *IEEE Electron Device Lett.*, vol. 35, no. 2, pp. 265–267, 2014.

[29] E. Kooi, J. G. Van Lierop, and J. A. Appels, “Formation of Silicon Nitride at a Si-SiO_2 Interface during Local Oxidation of Silicon and during Heat-Treatment of Oxidized Silicon in NH 3 Gas,” *J. Electrochem. Soc.*, vol. 123, no. 7, pp. 1117–1120, 1976.

[30] Y. Wang *et al.*, “Functionalized horizontally aligned CNT array and random CNT network for CO_2 sensing,” *Carbon N. Y.*, 2017.

[31] A. V. Kyrylyuk and P. van der Schoot, “Continuum percolation of carbon nanotubes in polymeric and colloidal media,” *Proc. Natl. Acad. Sci.*, 2008.

[32] J. S. Lee, J. H. Lee, and S. H. Hong, “NASICON-based amperometric CO_2 sensor using Na_2CO_3-$BaCO_3$ auxiliary phase,” *Sensors Actuators, B Chem.*, 2003.

[33] H. J. Shin, S. H. Kim, K. Park, M. C. Lim, S. W. Choi, and G. Ok, “Free-standing guided-mode resonance humidity sensor in terahertz,” *Sensors Actuators, A Phys.*, 2017.

[34] J. Wang, S. Wang, Q. Xin, and Y. Li, “Perspectives on water-facilitated CO_2 capture materials,” *Journal of Materials Chemistry A*. 2017.

[35] H. Yang, S. Xu, L. Jiang, and Y. Dan, “Thermal decomposition behavior of poly (vinyl alcohol) with different hydroxyl content,” *J. Macromol. Sci. Part B Phys.*, 2012.

[36] Y. ; Tsuchiya and K. Sumi, “Thermal decomposition products of poly(vinyl alcohol),” *J. Polym. Sci.*, 1970.

[37] M. Es-Saheb and A. Elzatahry, “Post-heat treatment and mechanical

assessment of polyvinyl alcohol nanofiber sheet fabricated by electrospinning technique," *Int. J. Polym. Sci.*, 2014.

[38] A. J. Page, F. Ding, S. Irle, and K. Morokuma, "Insights into carbon nanotube and graphene formation mechanisms from molecular simulations: A review," *Reports on Progress in Physics*. 2015.

[39] R. S. Park *et al.*, "Hysteresis in Carbon Nanotube Transistors: Measurement and Analysis of Trap Density, Energy Level, and Spatial Distribution," *ACS Nano*, 2016.

[40] D. D. Freeman, K. Choi, and C. Yu, "N-Type Thermoelectric Performance of Functionalized Carbon Nanotube-Filled Polymer Composites," *PLoS One*, 2012.

[41] D. D. K. D. D. K. Schwartz, "Mechanisms and kinetics of self-assembled monolayer formation," *Annu. Rev. Phys. Chem.*, 2001.

[42] Y. Sun, M. Yanagisawa, M. Kunimoto, M. Nakamura, and T. Homma, "Estimated phase transition and melting temperature of APTES self-assembled monolayer using surface-enhanced anti-stokes and stokes Raman scattering," *Appl. Surf. Sci.*, 2016.

[43] M. J. Pirouz, M. H. Beyki, and F. Shemirani, "Anhydride functionalised calcium ferrite nanoparticles: A new selective magnetic material for enrichment of lead ions from water and food samples," *Food Chem.*, 2015.

[44] D. V. Quang *et al.*, "Preparation of amino functionalized silica micro beads by dry method for supporting silver nanoparticles with antibacterial properties," *Colloids Surfaces A Physicochem. Eng. Asp.*, 2011.

[45] L. J. Mayne, S. D. R. Christie, and M. Platt, "A tunable nanopore sensor for the detection of metal ions using translocation velocity and biphasic pulses," *Nanoscale*, 2016.

[46] M. Terracciano, I. Rea, J. Politi, and L. De Stefano, “Optical characterization of aminosilane-modified silicon dioxide surface for biosensing,” *J. Eur. Opt. Soc.*, 2013.

[47] E. T. Vandenberg *et al.*, “Structure of 3-aminopropyl triethoxy silane on silicon oxide,” *J. Colloid Interface Sci.*, 1991.

[48] Y. Liang, J. Huang, P. Zang, J. Kim, and W. Hu, “Molecular layer deposition of APTES on silicon nanowire biosensors: Surface characterization, stability and pH response,” *Appl. Surf. Sci.*, 2014.

[49] N. S. K. Gunda, M. Singh, L. Norman, K. Kaur, and S. K. Mitra, “Optimization and characterization of biomolecule immobilization on silicon substrates using (3-aminopropyl)triethoxysilane (APTES) and glutaraldehyde linker,” *Appl. Surf. Sci.*, 2014.

[50] K. Shimanoe, K. Goto, K. Obata, S. Nakata, G. Sakai, and N. Yamazoe, “Development of FET-type CO_2 sensor operative at room temperature,” *Sensors Actuators B Chem.*, vol. 102, no. 1, pp. 14–19, Sep. 2004.

[51] P. Sedlak *et al.*, “Current fluctuation measurements of amperometric gas sensors constructed with three different technology procedures,” *Metrol. Meas. Syst.*, 2016.

[52] J. Shin *et al.*, “Highly improved response and recovery characteristics of Si FET-type gas sensor using pre-bias,” in *Technical Digest - International Electron Devices Meeting, IEDM*, 2017.

[53] C. Yu, A. Murali, K. Choi, and Y. Ryu, “Air-stable fabric thermoelectric modules made of N- and P-type carbon nanotubes,” *Energy Environ. Sci.*, 2012.

[54] A. Star, T. R. Han, V. Joshi, J. C. P. Gabriel, and G. Grüner, “Nanoelectronic carbon dioxide sensors,” *Adv. Mater.*, 2004.

[55] C. Kim, S. Pavlidis, M. G. Kim, O. Brand, and H. Chen, “Room temperature CO_2 detection using interdigitated capacitors with heteropolysiloxane sensing films,” in *Proceedings of IEEE Sensors*, 2017.

[56] K. G. Ong and C. A. Grimes, “A carbon nanotube-based sensor for CO_2 monitoring,” *Sensors*, 2001.

[57] E. Andreoli, L. Cullum, and A. R. Barron, “Carbon dioxide absorption by polyethylenimine-functionalized nanocarbons: A kinetic study,” *Ind. Eng. Chem. Res.*, 2015.

[58] Y. Taur and T. H. Ning, *Fundamentals of Modern VLSI Devices*. 1998.

[59] N. Lago *et al.*, “A physical-based equivalent circuit model for an organic/electrolyte interface,” *Org. Electron. physics, Mater. Appl.*, 2016.

[60] M. S. Kang, A. Sahu, D. J. Norris, and C. D. Frisbie, “Supp Info: Size-dependent electrical transport in CdSe nanocrystal thin films.,” *Nano Lett.*, 2010.

[61] M. Waleed Shinwari, M. Jamal Deen, and D. Landheer, “Study of the electrolyte-insulator-semiconductor field-effect transistor (EISFET) with applications in biosensor design,” *Microelectron. Reliab.*, 2007.

초 록

지난 수십 년 동안 이산화탄소(CO_2)를 감지하고 제어하는 기술은 많은 관심을 받아왔다. 이산화탄소의 양을 감지하는 것은 대기의 질이 어떻게 변화하는지를 추적하는데 중요할 뿐만 아니라 관련 환경 연구에서도 중요하다. 또한 실내공기 내의 이산화탄소는 사람에게 질병을 유발할 수 있기 때문에 실내 이산화탄소 농도를 특정 기준 이하로 제어하는 것이 중요하다. 지금까지의 연구들은 낮은 비용, 작은 크기, 적은 전력 소비, 높은 신뢰성을 가진 CO_2 센서를 개발하기 위해 노력하였다. 뿐만 아니라 실리콘 CMOS 센서 처리회로와 호환 가능한 센서 어레이를 만들 수 있으며 휴대 가능한 전자 코 시스템(electronic nose system)에도 응용할 수 있는 집적 가능한 CO_2 센서의 수요도 증가하고 있다.

따라서 본 논문에서는 저온에서 작동하는 FET형 CO_2 센서를 제안하고 폴리비닐 알콜(PVA), 폴리에틸렌이민(PEI)로 코팅된 단일벽 탄소나노튜브(SWNT), 무기 Na^+ 이온 전도성 물질과 같은 다양한 종류의 감지 물질을 적용하였다. 감지 물질은 잉크젯 프린팅 공정을 사용하여 FET 센서 플랫폼에 증착되었다. 센서의 기본적인 전기적 특성과 CO_2 감지 특성을 측정하였다. 이와 관련된 감지 동작 원리를 설명하고 모델링하

였다. PVA와 PEI로 코팅된 단일벽 탄소나노튜브 CO_2 센서는 습도의 도움을 받아 상온(약 25ºC)에서 CO_2를 검출 할 수 있다. Na^+ 이온 전도성 물질을 가진 센서는 160ºC에서 CO_2를 검출 할 수 있다. 제안된 센서는 기존의 CO_2 센서에 비해 상대적으로 낮은 작동 온도를 갖는다. 또한 FET형 센서는 실리콘 CMOS 기술과 호환가능하다. 센서의 캘리브레이션을 편리하게 만들기 위해 플로팅 게이트 구조를 채택하였다. 다른 감지 물질들에 비해 Na^+ 이온 전도성 물질을 갖는 센서는 습도의 도움을 받지 않고 감지 가능하며 가장 안정한 감지 특성을 가진다. 또한 저온에서의 CO_2 검출에 매우 효과적일 것으로 기대된다.

주요어: 이산화탄소 센서, FET형 센서, 낮은 온도, 폴리머, 단일벽 탄소나노튜브, 나트륨 이온 전도성 물질.

학번 : 2015-30749

List of Publications

Journals

1. Seongbin Hong, Jongmin Shin, Yoonki Hong, **Meile Wu**, Dongkyu Jang, Yujeong Jeong, Gyuweon Jung, Jong-Ho Bae, Ho Won Jang, and Jong-Ho Lee, “Observation of physisorption in a high performance FET-type oxygen gas sensor operating at room temperature,” *Nanoscale*, Vol. 10, No. 37, pp. 18019-18027, Oct. 2018.
2. **Meile Wu**, Jongmin Shin, Yoonki Hong, Dongkyu Jang, Xiaoshi Jin, Hyuck-In Kwon, and Jong-Ho Lee, "An FET-type gas sensor with a sodium ion conducting solid electrolyte for CO_2 detection," *Sensors and Actuators B*, Vol. 259, pp. 1058-1065, Apr. 2018.
3. Jongmin Shin, Yoonki Hong, **Meile Wu**, Jong-Ho Bae, Hyuck-In Kwon, Byung-Gook Park, and Jong-Ho Lee, "An accurate and stable humidity sensing characteristic of Si FET-type humidity sensor with MoS_2 as a sensing layer by pulse measurement," *Sensors and Actuators B*, Vol. 258, pp. 574-579, Apr. 2018.
4. **Meile Wu**, Jongmin Shin, Yoonki Hong, Xiaoshi Jin, and Jong-Ho Lee, "Pulse Biasing Scheme for the Fast Recovery of FET-Type Gas Sensors for Reducing Gases," *IEEE Electron Device Letters*, Vol. 38, pp. 971-974, Jul. 2017.
5. Jongmin Shin, Yoonki Hong, **Meile Wu**, and Jong-Ho Lee, "A Wide Detection Range Mercury Ion Sensor Using Si MOSFET Having Single-Walled Carbon Nanotubes as a Sensing Layer," *IEEE Electron Device Letters*, Vol. 38, No. 7, pp. 959-962, July 2017.
6. Yoonki Hong, Won-Mook Kang, In-Tak Cho, Jongmin Shin, **Meile Wu**, and Jong-Ho Lee, "Gas-Sensing Characteristics of Exfoliated WSe_2 Field-Effect Transistors," *Journal of Nanoscience and Nanotechnology*, Vol. 17, No. 5,

pp. 3151-3154, May 2017.

7. **Meile Wu**, Chang-Hee Kim, Jongmin Shin, Yoonki Hong, Xiaoshi Jin, Jong-Ho Lee, "Effect of a pre-bias on the adsorption and desorption of oxidizing gases in FET-type sensor," *Sensors and Actuators B: Chemical*, Vol. 245, pp. 122-128, Jan. 2017.
8. Xiaoshi Jin, **Meile Wu**, Xi Liu, Jung-Hee Lee, Jong-Ho Lee, "Optimization of saddle junctionless FETs for extreme high integration," *Journal of Computational Electronics*, Vol. 15, No. 3, pp. 801-808, Sep. 2016.

Conferences

1. Yujeong Jeong, Jongmin Shin, Yoonki Hong, **Meile Wu**, Seongbin Hong, Dongkyu Jang, Ki Chang Kwon, Seokhoon Choi, Ho Won Jang, and Jong-Ho Lee, “Suppression of Drift in FET-type Gas Sensor Having WS_2 Nanoparticles Using Pulse Measurement,” *International Meeting on Chemical Sensors (IMCS)*, Jul. 2018.
2. Seongbin Hong, Jongmin Shin, Yoonki Hong, **Meile Wu**, Yujeong Jeong, Jong-Ho Bae, and Jong-Ho Lee, “A Novel FET-type Hydrogen Gas Sensor with Pd-decorated Single-Walled Carbon Nanotubes by Electroplating Method,” *International Meeting on Chemical Sensors (IMCS)*, Jul. 2018.
3. **Meile Wu**, Jongmin Shin, Yoonki Hong, Dongkyu Jang, Xiaoshi Jin, and Jong-Ho Lee, “Inkjet-Printed PEI FET-Type Humidity Sensor Having a Horizontal Floating-Gate,” *International Meeting on Chemical Sensors (IMCS)*, Jul. 2018.
4. **Meile Wu**, Yoonki Hong, Dongkyu Jang, Xiaoshi Jin, and Jong-Ho Lee, “An FET-Type Gas Sensor for CO_2 Detection at Room Temperature Using PEI-Coated SWNT,” *Asia-Pacific Workshop on Fundamentals and Applications of Advanced Semiconductor Devices (AWAD)*, Jul. 2018.
5. Seongbin Hong, Jongmin Shin, Yoonki Hong, **Meile Wu**, Dongkyu Jang,

Yujeong Jeong and Jong-Ho Lee, "Humidity-sensitive Field Effect Transistor with In_2O_3 Nanoparticles as a sensing layer," *The Korean Sensors Society*, Feb. 2018.

6. Yujeong Jeong, Jongmin Shin, Yoonki Hong, **Meile Wu**, Seongbin Hong, and Jong-Ho Lee, "Gas Sensing Characteristics of the FET-type gas sensor having inkjet-printed WS_2 sensing layer," *The Korean Sensors Society*, Feb. 2018.

7. **Meile Wu**, Jongmin Shin, Yoonki Hong, Dongkyu Jang, Seongbin Hong, Yujeong Jeong, and Jong-Ho Lee, "An FET-type sensor with Pt doped In_2O_3 nanoparticles for room temperature hydrogen sensing," *The Korean Sensor Society*, Nov. 2017.

8. Yujeong Jeong, Jongmin Shin, Yoonki Hong, **Meile Wu**, Seongbin Hong, and Jong-Ho Lee, "Common Source Amplifier Circuit Integrated with the Gas Sensor," *The Korean Sensor Society*, Nov. 2017.

9. Seongbin Hong, Jongmin Shin, Yoonki Hong, **Meile Wu**, Dongkyu Jang, Yujeong Jeong, Hyuck-in Kwon, and Jong-Ho Lee, "Si FET-type gas sensor with a horizontal floating gate structure for detecting carbon monoxide," *The Korean Sensor Society*, Nov. 2017.

10. Jongmin Shin, Yoonki Hong, **Meile Wu**, Byung-Gook Park, and Jong-Ho Lee, "Response characteristics of Si FET-type humidity sensor having sputtered MoS_2 film as a sensing layer," *Korean Conference on Semiconductors*, Feb. 2017.

11. **Meile Wu**, Jongmin Shin, Yoonki Hong, Xiaoshi Jin and Jong-Ho Lee, "Effect of APTES Layer on I-V Characteristics of MOSFET-type Gas Sensor Having Solid Electrolyte Sensing Material," *NANO Korea*, Jul. 2016.

12. Yoonki Hong, Won-Mook Kang, In-Tak Cho, **Meile Wu**, and Jong-Ho Lee, "Gas-sensing characteristics of exfoliated WSe_2 field-effect transistors,"

Korean Conference on Semiconductors, Feb. 2016.

13. Jongmin Shin, Yoonki Hong, **Meile Wu**, Younjin Jang, Jun Shik Kim, Byung-Gook Park, Cheol Seong Hwang, and Jong-Ho Lee, "Highly Improved Response and Recovery Characteristics of Si FET-type Gas Sensor Using Pre-bias," *2016 International Electron Devices Meeting*, pp. 18.1.1-18.1.4, Dec. 2016.
14. Jongmin Shin, Yoonki Hong, **Meile Wu** and Jong-Ho Lee, "Sensing characteristic of lead ion using Si pMOSFET sensor under the different control-gate biases," *The 16th International Meeting on Chemical Sensors*, Jul. 2016.
15. Yoonki Hong, Jongmin Shin, **Meile Wu**, Soo Ho Choi, Yunsik Choi, Seungil Moon, Woochul Yang and Jong-Ho Lee, "MOSFET-based humidity sensor with inkjet-printed polymer as a sensing layer," *The 16th International Meeting on Chemical Sensors*, Jul. 2016.
16. Jong-Ho Lee, Yoonki Hong, **Meile Wu** and Jongmin Shin, "High Perfomance Gas Sensors Based on Si MOSFETs," *The 16th International Meeting on Chemical Sensors*, Jul. 2016.

Honors

1. Young Researcher Award, The 26th Asia-Pacific Workshop on Fundamentals and Applications of Advanced Semiconductor Devices (AWAD 2018), Kitakyushu, Japan, Jul. 2018.
2. Best Paper Award, 2016 Korean Sensor Society Conference, Korea, Nov. 2016.